EXPERIMENTAL INVESTIGATION OF NANOFLUID OSCILLATING HEAT PIPES

A Thesis presented to the Faculty of the Graduate School

University of Missouri – Columbia

In Partial Fulfillment

Of the Requirements for the Degree

Master of Science

By

COREY A. WILSON

Dr. Hongbin Ma, Thesis Supervisor

December 2006

The undersigned, appointed by the dean of the Graduate School, have examined the thesis entitled

Experimental Investigation of Nanofluid Oscillating Heat Pipes

presented by Corey Wilson,

a candidate for the degree of master of science,

and hereby certify that, in their opinion, it is worthy of acceptance.

Professor Hongbin Ma

Professor James Bryan

Professor Qingsong Yu

DEDICATION

To my parents for their encouragement throughout my education.

ACKNOWLEDGEMENTS

I would like to acknowledge several people who aided my research. Dr. Ma for sharing his expertise, and his encouragement and direction in my graduate research. Dr. Park and Dr. Han for their help implementing the transient hot wire method. Dr. Winholtz for his help and guidance on using neutron radiography to image oscillating heat pipes. And Brian Borgmeyer for his help with designing and testing heat pipes.

EXPERIMENTAL INVESTIGATION OF NANOFLUID OSCILLATING HEAT PIPES

Corey A. Wilson

Dr. Hongbin Ma, Thesis Supervisor

ABSTRACT

An experimental investigation was conducted of oscillating heat pipes (OHP) charged with diamond nanofluid. By combining the high thermal conductivity of nanofluids with the high heat transport rate of OHPs, a new type of heat pipe was developed. The diamond nanofluid used in this experiment was a combination of 5-50 nm diamond nanoparticles and a base fluid of high performance liquid chromatography (HPLC) grade water. The nanofluid thermal conductivity was found to be 1.00 W/m-K this is a 67% increase compared to HPLC grade water. It was shown that the OHP thermal resistance decreased from 0.75 °C/W with HPLC grade water to 0.49 °C/W with diamond nanofluid at an operating temperature of 20 °C and a heat load of 50 W, which is a 34% improvement in thermal resistance. Also by increasing the temperature, the OHP performance increased substantially. However, the difference between the nanofluid and the base fluid at higher temperatures was less significant. Even so, a thermal resistance of 0.03 °C/W was achieved at 336 W and with an operating temperature of 70 °C. Fluid frequency and amplitude were observed, via neutron radiography, to increase at increased temperatures and increased heat flux. Also, for the same heat flux and operating temperature, the water OHP had a slightly higher frequency and amplitude than the nanofluid OHP. Both of these trends match the temperature trends observed with the thermocouples.

TABLE OF CONTENTS

LIST OF FIGURES

LIST OF TABELS

NOMENCLATURE

A	Atomic weight (amu), total cross-sectional area (m^2)
a	Thermal Diffusivity (m^2/s)
b	Outer edge of measurement sample (m)
Bo	Bond number
c_p	Thermal capacitance (J/kg-K)
D	Diameter (m)
d	Thickness (m)
g	Gravitational acceleration (m/s^2)
g_v	Roots of $J(g_v)=0$
I	Intensity (W)
i	i^{th} element of the molecule
J	Bessel function
k	Thermal conductivity (W/m-K)
N_A	Avogadro's Number (molecules/mol)
q	Heat flux per unit length (W/m)
Q	Heat transfer rate (W)
r	Radius (m)
R	Thermal resistance (K/W), Electrical resistance (Ohm)
T	Temperature (°C)
t	Time (s)
T_c	Average temperature in the condenser (°C)
T_e	Average temperature in the evaporator (°C)
U	Overall heat transfer coefficient (W/m^2-K)
V_{IN}	Applied voltage (V)
V_{OUT}	Measured voltage (V)
w	Weight fraction

Y Bessel function

Greek

α Change in electrical resistance with respect to temperature

γ Euler's constant

ρ Density (kg/m^3)

σ Surface tension (N/m)

σ_i Neutron cross-section of the i^{th} element (barns)

Subscript

0 Original

c Condenser

e Evaporator

l Liquid

v Vapor

w Wire

CHAPTER 1

INTRODUCTION AND LITERATURE REVIEW

In the electronics industry and many other fields, devices are continually shrinking in size while their performance is continually increasing. This generally leads to concentrated heat flows which are very damaging to many devices and must be removed. Over the years, many cooling technologies have been developed to remove the heat. One device that shows promise is the oscillating heat pipe (OHP). The OHP was invented and patented in 1990 by Akachi [1]. Because the OHP can transfer high heat load and can be manufactured in almost any shape and a low cost, the OHP will play a key role in the electronics cooling. The operating mechanism of OHPs is the vaporization, condensation and thermal expansion of a working fluid as a driving force to transfer heat.

Nanofluid Characteristics

Fluids typically have very low thermal conductivity compared to solids and can therefore limit thermal performance in many situations. By improving this thermal conductivity, the thermal performance of many devices can be improved significantly. In 1995, Choi [2] predicted that nanofluids, a suspension of nanoparticles (less than 100 nm in diameter) in a liquid, could improve the thermal conductivity of the base fluid 3.5 times. Since then, numerous investigations have been carried out on the thermal behavior of nanofluids. Most of this work focused on the effective conductivity [3,4,5] and convective heat transfer of nanofluids [6,7]. Generally it has been found that increased volume percent (vol%) of nanoparticles in the base fluid results in an increase of thermal conductivity.

When nanoparticles are added to the base fluid the nanoparticles will remain suspended or settle out of solution depending on the base fluid and other added stabilizers. In one instance, Eastman et al. [8] measured the thermal conductivity of copper nanoparticles with a glycol base fluid. Some settling occurred, so a small amount of thioglycolic acid was added. Fewer nanoparticles settled and the thermal conductivity greatly increased.

Oscillating Heat Pipe Operation and Design Considerations

An OHP consists of a small diameter channel or tube that crosses a condenser and evaporator region multiple times (Fig. 1.1). This tube is filled with a fluid at a certain fill ratio (fluid volume/total internal volume), and is filled such that only the fluid and its vapor phase exist. The tube's inner diameter must also be small enough for the capillary forces of the fluid to create vapor bubbles (plugs) and liquid slugs. In this way the vapor plugs completely block the flow of the liquid. This keeps the plugs and slugs in a linear arrangement within the tube as can be seen in Fig. 1.1. Heat is transferred through the OHP via pressure induced motion of this liquid and vapor. Evaporation at a higher temperature in the evaporator produces a higher vapor pressure. The same is the case for the condenser where condensation and reduced temperature at the condenser cause a decrease in pressure. This increased pressure in the evaporator and lowered pressure within the condenser causes a pressure imbalance. Due to the typically random arrangement of slugs and plugs within an OHP, this pressure imbalance forces the hot vapor and fluid from the evaporator to the condenser and conversely the cool vapor and fluid from the condenser to the evaporator, resulting in an oscillating motion. The

oscillating motion consists of small rapid movement within portions of the tube and in some cases bulk motion through the entire OHP.

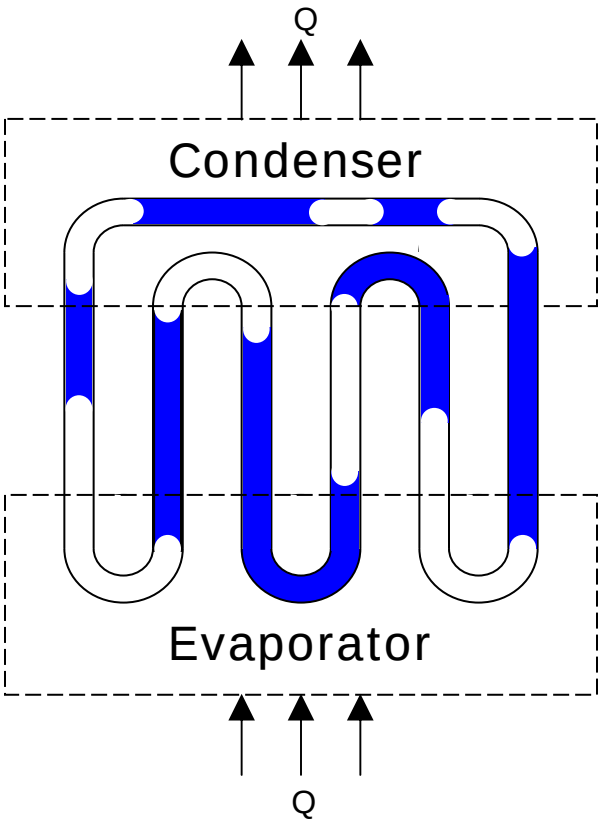

Fig. 1.1. Schematic of a typical OHP with multiple turns (The black and white regions represent the fluid and gas phases respectively)

There are two general types of OHP, open and close looped. The close looped OHP is a continuous tube that crosses the evaporator and condenser multiple times (Fig. 1.1). The open looped OHP is similar except the two ends of the tube are sealed. The key difference between the two types of OHPs is that the fluid within close looped OHP can flow continuously through the tube. Generally, close looped OHPs perform better than open looped [9].

Most OHP are constructed out of copper, aluminum, glass and/or plastic. Copper and aluminum with their high conductance, are better suited for recording the transient temperatures within the OHP and are closer to materials which would be used in production devices. Glass and plastic have been used in several experiments for visual observation of the fluid flow [10,11,12,13,14,15].

Typically OHPs have a design similar to the one shown in Fig. 1.1 where the fluid channel is a tube that remains in one plane. Other OHP designs utilize a 3D pattern or instead of tubing use channels in a metal plate. The 3D tubing pattern, where tubing is bent into multiple planes, enables the OHP to work better in the horizontal orientation. It also can allow for a much higher turn density. This type of OHP is harder to model because the gravitational vector changes along the tube. Flat-plate OHPs utilizes a plate or sheet with the fluid channels stamped or machined into it. Because of this, it has the prospect of being very simple to manufacture. Compared to a tube OHP, the flat plate OHP can fit more turns into a smaller size. This is because there is a minimum bend radius for a tube, whereas a channel can be cut into a much smaller bend radius. It should be noted that typically in this design heat can conduct from one channel to the next through the adjoining wall. This makes the OHP very difficult to model mathematically.

While the shape of an OHP generally remains the same between studies, the number of turns and the length of the evaporator, adiabatic, and condenser sections usually differ. Because of the complex nature of their operation these differences make it difficult to compare results. The number of turns plays a significant roll in how an OHP works. Khandekar et al. [13] studied a single turn OHP and found that due to gravity it would not work at angles of less than 10º to horizontal and even during larger angles it

would sometimes stop working. In this case, a bubble would stop over the evaporator and dry-out would occur causing a complete stop in motion in the OHP and an increase in the thermal resistance. This occurred more frequently for fill ratios of less than 50% and was found not to be as common in multi-turn OHPs.

A crucial design constraint of OHPs is the internal tube diameter. The internal diameter of an OHP must be small for vapor bubbles to span the diameter of the tube. If the internal diameter is too large the water and vapor will stratify in the OHP. The expanding and contracting vapor bubbles would no longer push the fluid through the tube. As long as the hydraulic diameter remains within this limit, increasing the diameter generally increases the overall heat transport capability of the OHP [16]. The maximum hydraulic diameter is,

$$D_{\max} = \sqrt{\frac{Bo_{crit}\sigma}{g(\rho_l - \rho_v)}} \tag{1.1}$$

where Bo_{crit} is the critical bond number, σ is the surface tension, ρ_l is the liquid density, ρ_v is the vapor density, and g is the gravitational acceleration. There is a slight dispute on the critical bond number, Shafii et al. [17] use a critical Bond number of 1.84 while Khandekar et al. [18] use the value of 2 to determine the minimum tube diameter. In this current investigation, a Bond number of 1.84 is used to determine the inside diameter of the tube.

The fill ratio is another very important parameter of the OHP. If the fill ratio is too low, the fluid in the evaporator could completely evaporate at low heat loads, this phenomenon is called dry-out. Dry-out can occur at high fill ratios if the temperature of

the heat pipe is above the critical temperature for that fill ratio. If the fill ratio is too high, the OHP vapor plugs cannot grow large enough to sustain slug and plug flow. Table 1.1 presents a list of experimentally determined working fill ratios.

Table 1.1. Literature review of working fill ratio.

Working Fluid	Working Fill Ratio (%)
Water	40-50 [12] 72.2 [19] 60-70 [20] 30-50 [21]
Acetone	40-50 [12]
Ethanol	60-70 [20,19] 30-50 [21]
Alcohol	40-50 [12]
Ammonia	40-70 [12]
FC-72	72.6 [19] ~70 [10] 50 [14]

Gravitational orientation also has a very significant affect on OHPs. A study by Khandekar et al. [13] found that their single turn OHP would not work at angles less than 10º to horizontal with the heater on the gravitationally lower end of the OHP. They explain that before heat was applied the OHP, the vapor bubbles were randomly arranged and once evaporation occurred within the OHP, the gravitational and wall shear stress created a path of least resistance to the condenser. In horizontal operation where gravity

does not create a pressure gradient, there is no preferential direction for the bubble to move, therefore, it does not move. While single turn OHPs do not work horizontally, multi-turn OHPs do work horizontally, but at a greatly increased thermal resistance [11, 13]. One contradictory study [22] found that a flat-plate 40 turn OHP was stable in all orientations, even top heating in a vertical orientation. This however could be due to the large number of turns.

During the start-up period, an OHP behaves differently than during normal operation. This is because until the pressure difference within the OHP is sufficient, the fluid slugs and vapor bubbles remain stationary. Without this fluid motion, heat is transferred via conduction through the OHP tubing, liquid, and vapor. This can result in a large initial temperature difference between the evaporator and the condenser. Once fluid motion begins, this temperature difference decreases.

Xu et al. [10] studied the start-up transient characteristics of the OHP at low and high thermal loads. At low thermal loads (10 W, FC-72 working fluid), the start-up period lasted several minutes with an overshoot of 10 ºC. Once the fluid motion started, the temperature difference immediately reduced. At high thermal loads (25 W, FC-72 working fluid), the start-up period temperature difference profile much smoother but the temperature difference continued to rise after oscillations began.

Similar to startup, at low heat loads, the pressure difference is not large enough to cause oscillation. Zhang et al. [19] studied this phenomenon with three fluids, FC-72, ethanol, and deionized water. The lowest minimum heat power to initiate oscillations was found to be 18 W for water, 10 W for ethanol and 8 W for FC-72.

During normal operation of an OHP, the temperature in the evaporator and condenser fluctuate rapidly. The fluctuating temperatures are due to movement of the liquid slugs and vapor plugs. Much theoretical and experimental research has been conducted to determine and predict this motion. One such experiment by Khandekar et al. [10] utilized a high-speed camera to observe the flow patterns within a glass OHP. When the OHP was initially charged, liquid slugs and vapor plugs formed randomly throughout the tube. After heat was applied, bubble nucleation started in the evaporator, increasing the pressure within the OHP. Some of the new bubbles and the existing vapor plugs coalesced. The vapor plugs in the condenser section condensed due to the increased pressure within the OHP. The bubble creation, coalescence, and condensation caused the pressures within the OHP to change rapidly. During start-up, this caused the existing vapor plugs to oscillate at increasing rates. Initially, the oscillations were centered on a stationary or nearly stationary point. Eventually, bulk flow through the entire OHP occurred. This bulk flow did switch directions but with a much longer period than the short oscillations of the bubbles. This oscillation motion varied between working fluids. For methanol, the displacements and velocities followed a quasi-sine pattern, while water had periods of fast movement and then no movement. Water's intermittent motion was attributed to its large latent heat of evaporation.

CHAPTER 2

THERMAL CONDUCTIVITY MEASUREMENT OF NANOFLUIDS

Many methods of measuring thermal conductivity of liquids have been developed. Most methods attempt to approximate one dimensional or radial conduction models utilizing either steady-state or transient heat transfer and a few approximate spherical conduction models. All of these models are very difficult to approximate experimentally. For instance, the one dimensional steady state model applies to a test sample that has a finite thickness, but is infinitely wide in the x and y directions. Through this finite thickness a constant heat flux must be applied. Because it is impossible to create an infinitely wide device, a lesser width must be used to approximate infinity. Also, theoretically, the thickness of the sample must be constant over the entire width, this can be very difficult to accurately achieve in the real world, especially if the sample is thin. And lastly, applying a perfectly uniform heat flux to the sample is very difficult. All of these approximations must be accounted for by calibrations and calculations. Measuring the thermal conductivity of fluids has an additional difficulty. A temperature difference across a fluid creates a density gradient as well. This density gradient causes convection, which alters any measured thermal conductivity. Several approaches to this problem have been developed. One method is to make the layer of fluid so thin that convection does not significantly alter the thermal conductivity. This method is typically used for steady-state devices. The other method of thermal conductivity measurement involves starting with a stationary fluid, applying a heat flux and taking the measurement before convection occurs. A transient method that works on this principle is called the transient hot-wire method. It employs a metal wire to approximate a line heat source and measure

the thermal conductivity. The wire is sufficiently long so that it can be approximated as an infinitely long heat source. The wire must also be sufficiently thin so the line heat source model remains valid. Heat is generated by applying an electrical current to the wire. This current generates heat through resistive heating. The heat in the wire is conducted away via thermal conduction through the fluid. The rate of heat removal from the wire determines the rate of temperature change of the wire. In turn, the electrical resistance of the wire is directly related to the temperature of the wire. Therefore, the change in resistance is related to the thermal conductivity of the surrounding fluid [23].

Transient Hot-Wire Theory

The transient hot-wire method is a well established method at measuring thermal conductivity of fluids. This method approximates transient radial conduction with thin wire suspended in the center of the sample. This method is favored because of the relatively short test time and simplicity of the experimental design. The relationship between the thermal conductivity and transient radial conduction is derived as follows [23,24]. Starting from the transient heat conduction model, i.e.,

$$\rho C_p \frac{\partial T}{\partial t} = k\nabla^2 T \tag{2.1}$$

and defining,

$$\Delta T(r,t) = T(r,t) - T(0,0) \tag{2.2}$$

The boundary conditions are,

$$\Delta T(r,t) = 0 \text{ at t=0} \tag{2.3}$$

$$\lim_{r\to 0}\Delta T(r,t)=0 \text{ for } t>0 \tag{2.4}$$

$$\lim_{r\to 0} r\frac{\partial T}{\partial r}=-\frac{q}{2\pi k}=\text{constant for } t\geq 0 \tag{2.5}$$

where r is the distance from the heat source, t is time, a is the thermal diffusivity which is defined as $a = k/\rho C_p$, and $T(0,0)$ is the equilibrium temperature. With the boundary and initial conditions described above, Eq. (2.1) can be solved and the resulting solution is,

$$\Delta T(r,t)=-\frac{q}{4\pi k}E_1\left(\frac{r^2}{4at}\right) \tag{2.6}$$

where,

$$E_1(x)=\int_x^\infty \frac{e^{-y}}{y}dy \tag{2.7}$$

By using series expansion, Eq. (2.6) can be simplified to,

$$\Delta T(r,t)=\frac{q}{4\pi k}\left(\ln\frac{4\alpha t}{r^2}-\gamma-\sum_{k=1}^{\infty}\frac{\left(\frac{r^2}{4\alpha t}\right)^k}{kk!}\right) \tag{2.8}$$

Solving Eq. (2.8) over a $t_2 - t_1$ is,

$$\Delta T(t_2-t_1)=\Delta T(r,t_2)-\Delta T(r,t_1) \tag{2.9}$$

and combining Eq. (2.8) and (2.9) results in,

$$\Delta T\left(t_2 - t_1\right) = \frac{q}{4\pi k}\ln\left(\frac{t_2}{t_1}\right) \tag{2.10}$$

Solving for thermal conductivity gives the thermal conductivity of the fluid,

$$k = \frac{q}{4\pi\Delta T\left(t_2 - t_1\right)}\ln\left(\frac{t_2}{t_1}\right) \tag{2.11}$$

This resulting equation provides a simple means of finding thermal conductivity as it is only dependent on heat flux from the wire, and the measured temperatures and time. However some of the assumptions that were used in this derivation can not be achieved in the real world. Equation (2.11) assumes that the heat source has zero radius where an actual wire resistance heater will have a finite radius, and that the fluid sample has an infinite radius and length which is impossible to attain. The error produced by these assumptions can be great depending on the diameter of the wire and size of the measurement medium. The wire's radius effect on the temperature difference [24] is,

$$\delta T_1 = \frac{q}{4\pi k}\left[\frac{r_w^2\left(\rho_w Cp_w - \rho Cp\right)}{2kt}\ln\frac{4at}{r_w^2 e^{\gamma}} - \frac{r_w^2}{2at} + \frac{r_w^2}{4a_w t} - \frac{k}{2k_w}\right] \tag{2.12}$$

and the radius of the fluid effect the temperature difference [24] is

$$\delta T_2 = \frac{q}{4\pi k}\left[\ln\frac{4at}{b^2 e^{\gamma}} - \sum_{\nu=1}^{0} e^{-g_\nu \frac{at}{b^2}}\left[\pi Y\left(g_\nu\right)\right]^2\right] \tag{2.13}$$

Based on the analysis presented above, the typical design of a transient hot-wire thermal conductivity cell is a chamber of sufficient size with a very thin wire of sufficient length stretched taunt across it. The wire acts as both the heat source and the temperature

sensor. This is possible because the resistance of metal is dependent only on the temperature of the wire. Therefore when a current is applied to the wire it generates heat and as this heat is conducted away from the wire the temperature of the wire changes resulting in a resistance change. Using this method, the voltage applied to the wire and the small resistance change of the wire must be measured. This is accomplished by attaching the wire to a Wheatstone bridge as shown in Fig. 2.1.

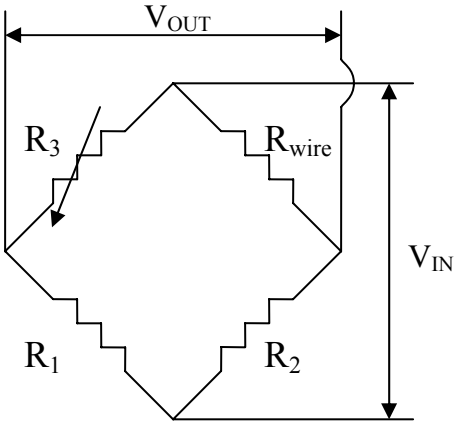

Fig. 2.1. The Wheatstone bridge used to determine the resistance of the platinum wire

Using the circuit shown in Fig. 2.1, the resistance of the wire is,

$$R_{wire} = R_2 \frac{\left(\frac{V_{OUT}}{V_{IN}} + \frac{R_3}{R_1 + R_3}\right)}{\left(1 - \frac{V_{OUT}}{V_{IN}} - \frac{R_3}{R_1 + R_3}\right)} \tag{2.14}$$

Using the linear relation between resistance and temperature, the temperature of the wire is,

$$T = \frac{1}{\alpha}\left(\frac{R_{wire,T}}{R_{wire,T=0°C}} - 1\right) \tag{2.15}$$

where α is defined as,

$$\alpha = \frac{\partial \frac{R_{wire}}{R_{wire,T=0°C}}}{\partial T} \tag{2.16}$$

Using Eqs. (2.14), (2.15), (2.16), and (2.11), the thermal conductivity of the fluid can be found.

Experimental Design

Based on the criteria of the line heat source model presented above, a transient hot-wire thermal conductivity cell was designed. A rectangular container was constructed so that the line heat source wire could be at least 10 cm long and would contain about 100 ml of fluid. Platinum was chosen for the line heat source material due to its low chemical reactivity and linear electrical resistance to temperature relationship. The container, shown in Fig. 2.2, was constructed out of 1.49 cm thick acrylic, assembled using methyl chloride. A 1.27 cm diameter hole was drilled in each end of the cell. A 10 cm length of pure platinum wire with a diameter of 0.0254 mm was attached to 1.59 mm diameter copper tube electrical leads. The end of each copper tube was first filed and polished to remove any sharp edges which might cut the platinum wire. The platinum wire was then inserted 1-2 cm into the copper tube and the tube was flattened over the wire, crimping it in place. The two copper tubes were inserted through rubber stoppers and the rubber stopper/platinum wire assembly was placed in the acrylic chamber holes. The platinum wire was adjusted until it was taunt and the rubber stoppers formed a tight

seal with the acrylic chamber. The portion of the copper tube that would be in contact with the measurement fluid was covered in RTV silicone to prevent galvanic corrosion between the copper and platinum. Electrical wire leads were soldered onto the copper tubing protruding outside the acrylic chamber. Additionally a type T thermocouple was placed in the chamber for calibration and monitoring purposes.

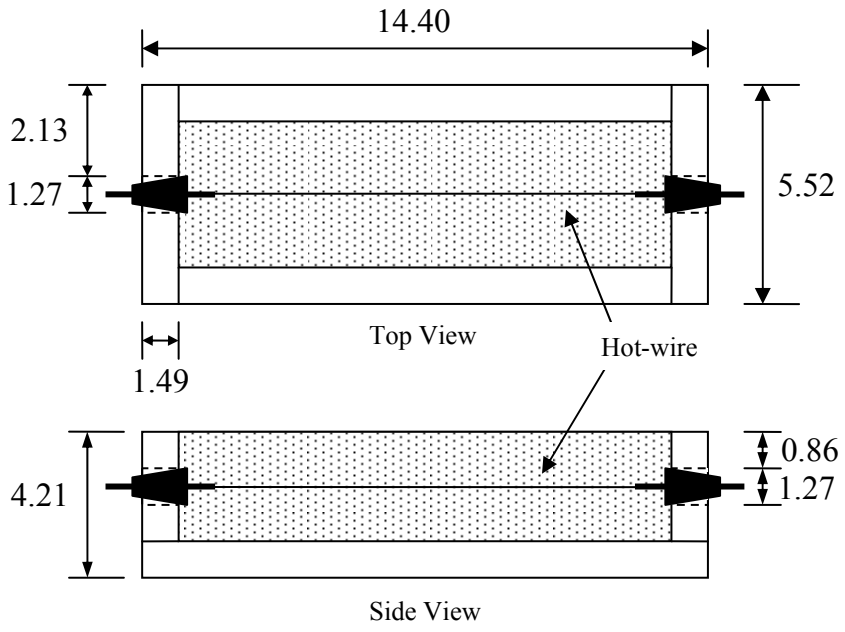

Fig. 2.2. A top and side view of the thermal conductivity test bed (Dimensions are in cm)

The resistance of the platinum wire was calibrated over a range of temperatures. This was accomplished by filling the container with HPLC grade water of varying temperatures. The resistance of the wire was measured using a Fluke 45 dual display multimeter and the water temperature was measured by a National Instruments SCXI-1600 DAQ with a T-type thermocouple. The resistances were then scaled using Eq. (2.16). These values follow a linear relation as shown in Fig. 2.3.

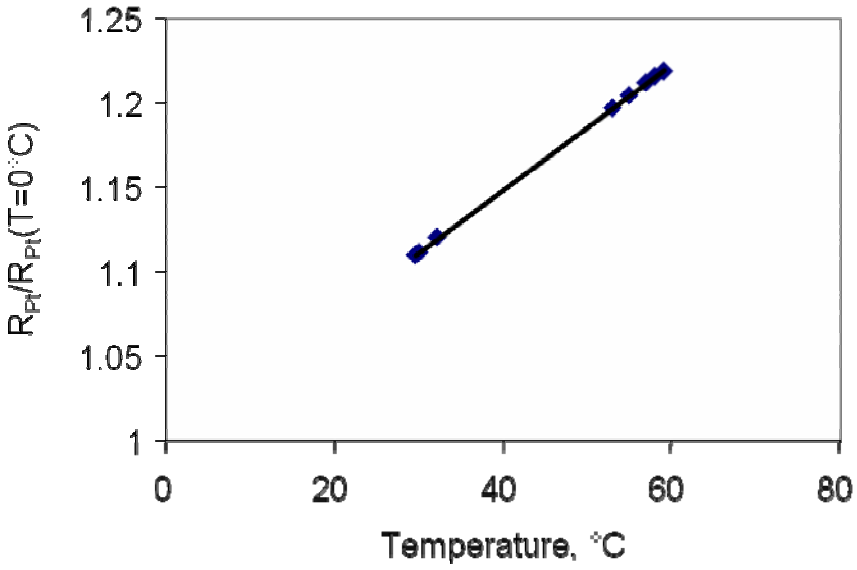

Fig. 2.3. The change in resistance with temperature scaled to the resistance at 0 °C.

To determine the change in resistance, the Wheatstone bridge shown in Fig. 2.1 was constructed. The input voltage of 5 V was supplied by an Agilent E3645A DC power supply and the output voltage was measured by a National Instruments SCXI-1600 DAQ. This data acquisition system was also used to measure the temperature of the liquid with the thermocouple. The data was collected at a rate of 500 samples per second. Each thermal conductivity test was conducted at ambient temperature for a duration of 131 seconds. Between tests the fluid was allowed to cool and equilibrate with the surroundings for several minutes. This experimental set-up can be seen in Fig. 2.4.

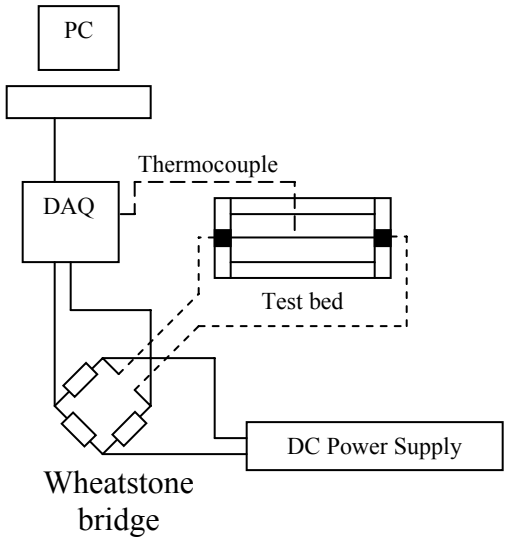

Fig. 2.4. Experimental set-up of the thermal conductivity experiment.

When the Wheatstone bridge was properly balanced, the resulting plot of voltage with respect to ln(t) had a portion with a linear positive slope which corresponds to the thermal conductivity of the fluid as shown Fig. 2.5. This portion was curve fit and using Eqs. (2.11) and (2.14)-(2.16) the thermal conductivity of the fluid was determined.

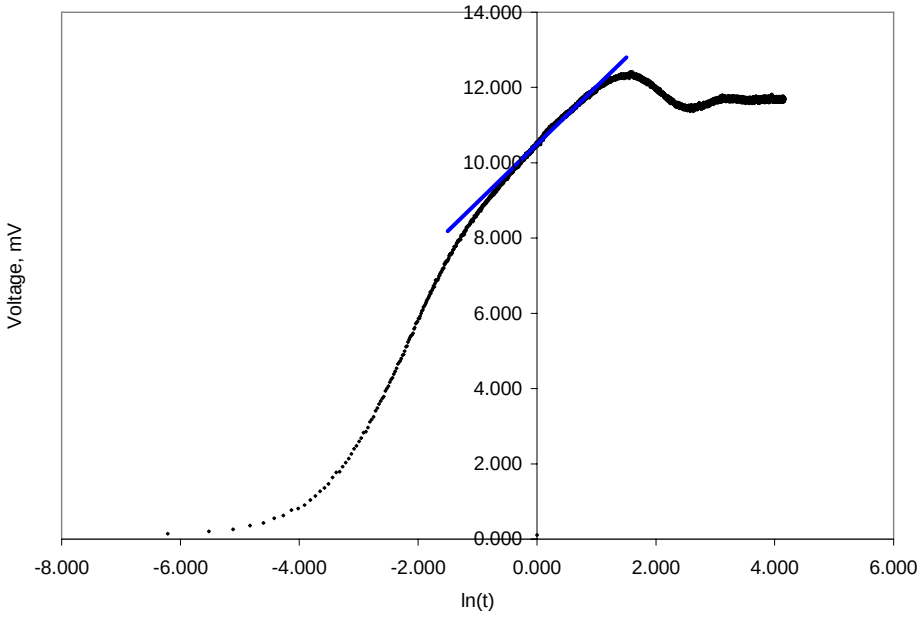

Fig. 2.5. The variation of output voltage with respect to ln(*t*).

Results and Discussion

The thermal conductivity of a baseline and the nanofluid in question were measured. The baseline, high purity liquid chromatography (HPLC) grade water, and diamond nanofluid were both measured at room temperature. The thermal conductivity of HPLC grade water was measured and compared with the known thermal conductivity (Table 2.1) [23]. The accuracy of the thermal conductivity measurement compared to the known thermal conductivity was 4 %. The theoretical error due to the wire thickness, using Eq. (2.12), was 0.32% and due to fluid thickness, using Eq. (2.13), was 3.5%. Then using the same experimental setup, the thermal conductivity of diamond nanofluid was measured. The diamond nanofluid contained 1.0 vol.% (0.035 g/ml) diamond nanoparticles in HPLC grade water. The nanoparticle size was 5 – 50 nm fabricated by a 20 kW RF plasma with a frequency of 13.56 MHz. When the nanoparticles were added

to the water, most of the nanoparticles in the motionless water slowly fell out of solution as shown in Fig. 2.6. After the nanoparticles reached a steady suspension, the majority of the nanoparticles settled on the bottom, however the smaller particles remained suspended. A sample of these remaining suspended particles was measured using images captured with a tunneling electron microscope (Fig. 2.7). The size of the nanoparticles show that only the nanoparticles with a diameter less than 10 nm can be suspended in motionless water.

Table 2.1. Experimental data of thermal conductivities of water and nanofluid at 21.5 °C.

Water		Nanofluid
Measured	Accepted Value [23]	Measured
0.58 W/m-k	0.60 W/m-k	1.00 W/m-k

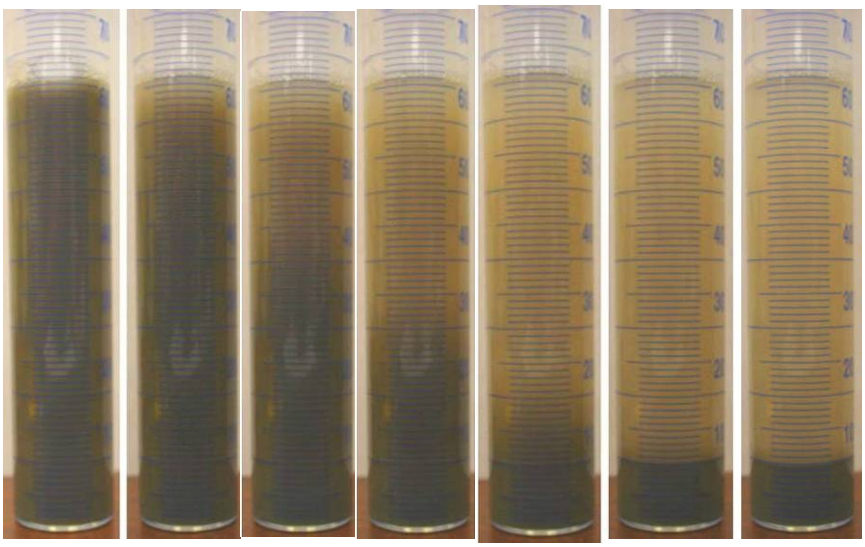

(a) (b) (c) (d) (e) (f) (g)

Fig. 2.6. The sedimentation of diamond nanoparticles at settling times of (a) 0 min, (b) 1 min, (c) 2 min, (d) 3 min, (e) 4 min, (f) 5 min, and (g) 6 min

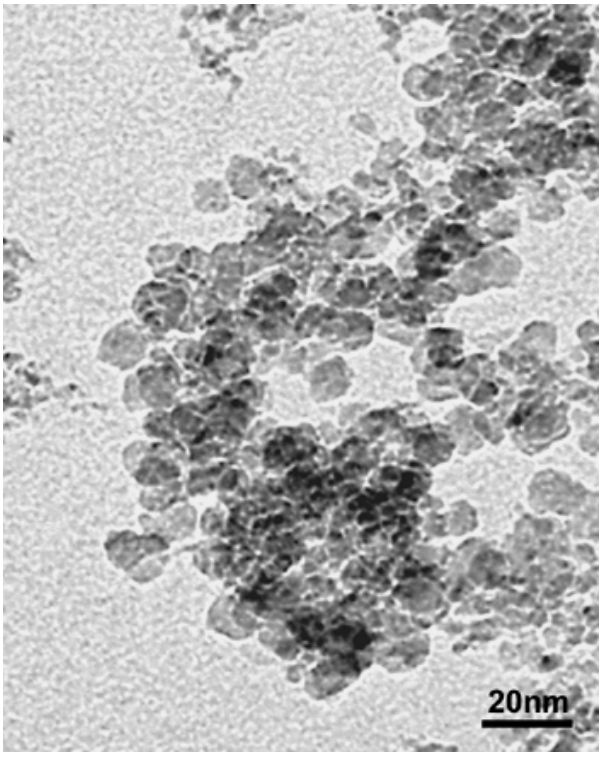

Fig. 2.7. Transmission electron microscopy image of diamond nanoparticles collected from suspended region of motionless nanofluid.

When using the transient hot-wire method to measure the thermal conductivity of a fluid, the fluid must be motionless. Therefore the transient hot-wire method can only measure the thermal conductivity of the diamond nanofluid that remains in suspension, in other words nanofluid with diamond nanoparticles less than 10 nm in diameter. Even so, the thermal conductivity of the motionless nanofluid increases from 0.60 W/m-k for HPLC grade water to 1.00 W/m-k for diamond nanofluid at 21.5 °C (Table 2.1). With only the 10 nm and less nanoparticles suspended in the water, the thermal conductivity increased by 67%. Similar results were found by Kang et al. [25] with their transient-hot wire measurement of diamond nanoparticles in ethylene glycol.

CHAPTER 3

EIGHT AND TWELVE TURN OSCILLATING HEAT PIPES

Oscillating Heat Pipe Design and Fabrication

Two different designs of closed loop OHPs were used to investigate the effect of nanofluid on their heat transfer performance. The first design was a 12-turn OHP (Fig. 3.1a) that was initially charged with water and then later with nanofluid. The second design was an 8-turn OHP (Fig. 3.1b). Two were 8-turn OHPs were built, one was charged with water and the other with nanofluid. Other than the number of turns, these three OHPs were designed and constructed essentially the same.

Considering commercial availability, Alloy 122 copper tubing with an inside diameter of 1.65 mm and an outer diameter of 3.18 mm was used for these OHPs. The tube's inner diameter was well within the constraints imposed by Eq. (1.1) for water as the operating fluid. The evaporator and condenser regions were both constructed out of 6.35 mm thick Alloy 122 copper sheets to spread the heat from the tubes to the heat source and sink. Using a ball end mill, 3.18 mm deep semi-circular grooves were machined in the plates. Omegabond '201' thermal paste was placed in the grooves and the copper tubing was inserted into these grooves. In this way, the tubes had a tight fit, low contact thermal resistance and a large contact surface area with the copper plates. For the 12 turn OHP, the evaporator plate had dimensions of 6 cm x 30.2 cm where a uniform heat flux was added on one side and the condenser had the same dimension where water cooled blocks were attached. The distance between the evaporator and the condenser was 10.2 cm. For the 8-turn OHP, the evaporator had dimensions of 3.8 cm x 20.3 cm and the condenser had dimensions of 6 cm x 20.3 cm with a distance of 10.2 cm

between. After the tubes were placed in the grooves, the two ends of the tubes and a 1.5 mm diameter copper tube were joined with a T-fitting. The 1.5 mm copper tube was the "charging tube" through which fluid was introduced into the OHP. The constructed OHPs are shown in Fig. 3.2.

All OHPs were charged to a fill ratio of 50%. This value was chosen because several studies [12,21] found that water charged OHPs worked at this fill ratio. The water OHPs were filled with HPLC grade water and the nanofluid OHPs were filled with the diamond nanofluid described in Chapter 2. The 12-turn OHP was charged with 1.0 vol% (0.035 g/ml) nanofluid after initial tests were conducted with water. The 8-turn nanofluid OHP was charged with 0.016 vol% (0.0005 g/ml).

The general procedure for charging an OHP was to place it on a scale and connect the charging tube to a vacuum pump. Air in the OHP was removed and the working fluid was then introduced into the OHP. The OHP was very slightly over filled and the excess fluid was removed by applying the vacuum pump a second time. This second vacuuming removed remaining non-condensable gas from the OHP and fluid. Once the correct volume percent was achieved, as indicated by the scale, the charging tube was sealed.

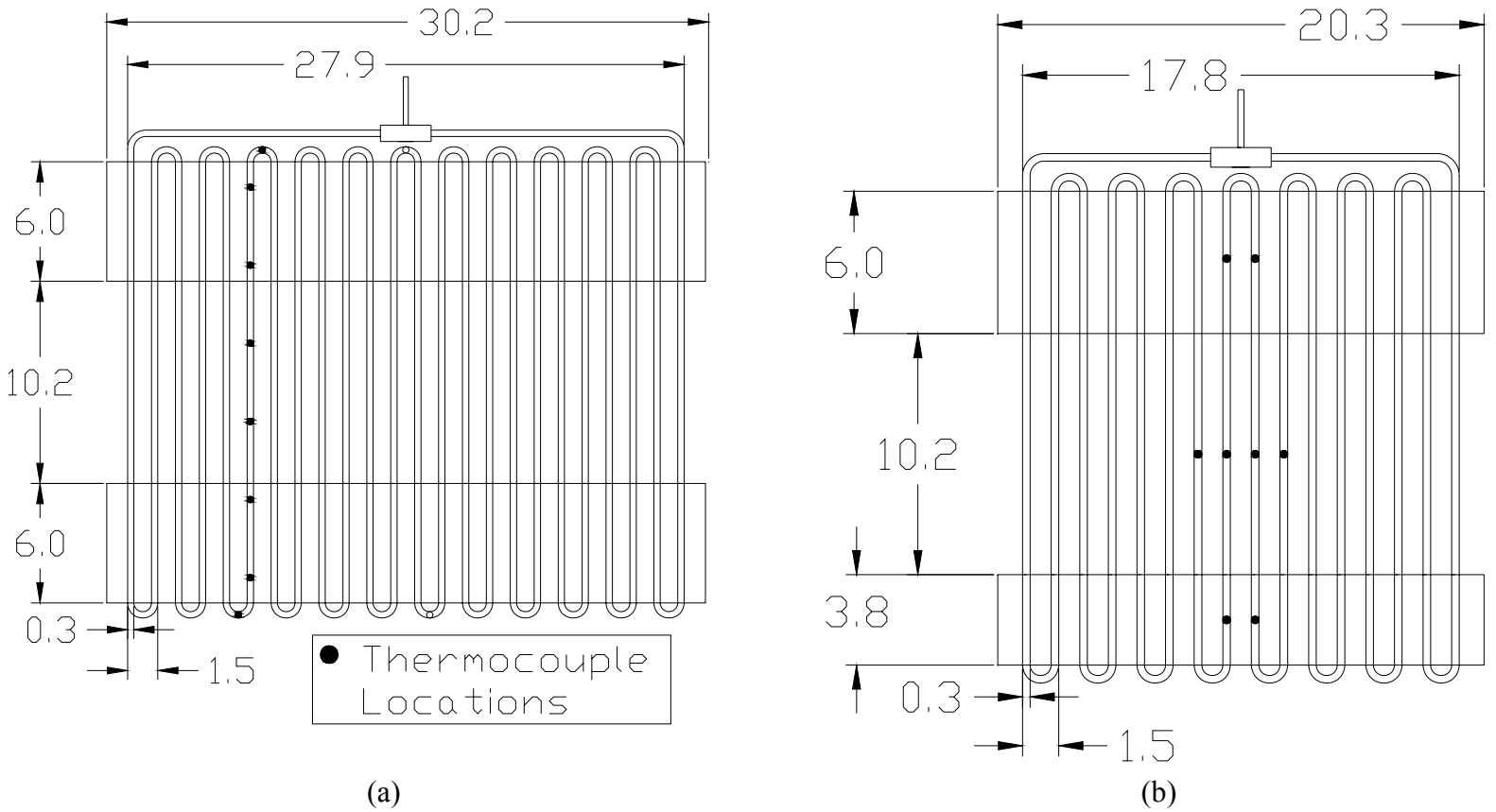

Fig. 3.1. Design and thermocouple locations of the (a) 12 turn OHP and (b) 8 turn OHPs (Dimensions are in cm).

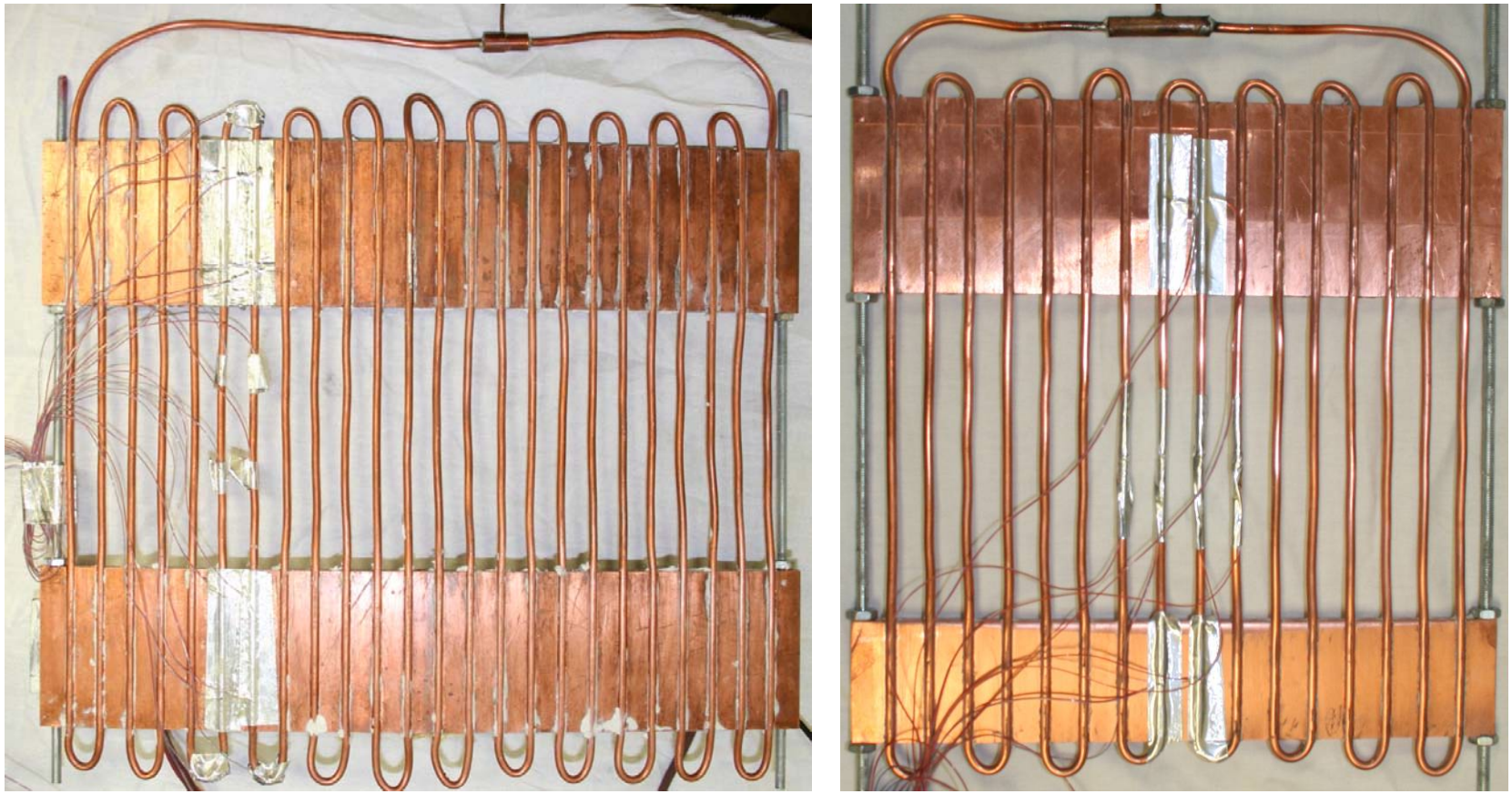

(a) (b)

Fig. 3.2. Pictures of the (a) 12 turn OHP and (b) 8 turn OHPs

Experimental Setup

Each OHP had the same experimental setup as shown in Fig. 3.3. A Tempco strip heater was attached to the evaporator plate and water cooled blocks were attached to the condenser plate. Thermal paste was used to improve contact thermal resistance. Temperature-controlled water was supplied to the condenser by a Julabo F34/MD circulator. Type T thermocouples were placed on the OHP in the locations shown in Fig. 3.1. A National Instruments SCXI-1600 data acquisition system and personal computer were used to record the temperatures. Power was supplied to the heater by a Staco 3PN501B voltage regulator and the voltage was measured by a Fluke 45 dual display multimeter. The entire OHP was surrounded by insulation to ensure heat transfer occurred only in the evaporator and condenser regions.

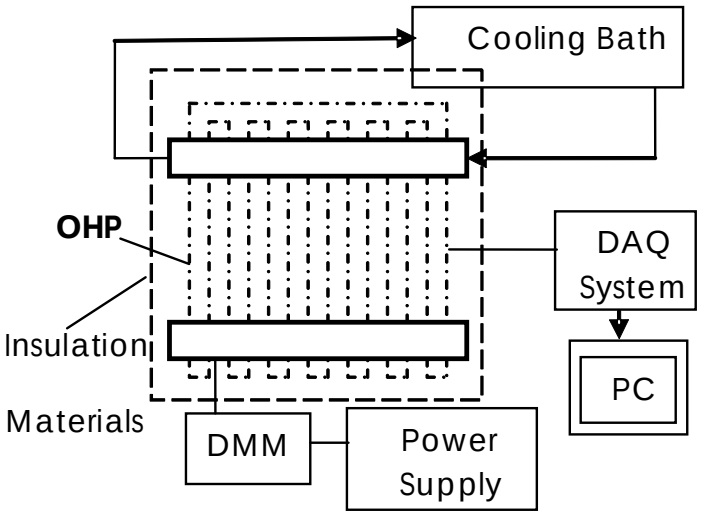

Fig. 3.3. Schematic of experimental setup

Prior to the start of the experiment, the system was allowed to equilibrate and reach steady-state such that the temperature of the heat pipe was constant at ± 0.5 °C over a 12-minute sample time. When the desired steady-state condition was obtained, the input power was increased in small increments. After each power increase, the OHP was allowed to reach steady state. During the tests, temperature data was collected at 100 samples/second.

Neutron Radiography Experimental Setup

In a separate experiment, video of the OHPs' fluid movements were recorded using neutron radiography. This experiment was performed at the National Institute of Standards and Technology (NIST) research reactor in Gaithersburg, Maryland with their neutron radiography experimental setup. Neutron radiography utilizes a beam of neutrons that pass through the imaging object and strike a detector. When the neutrons pass through the object, they are scattered and absorbed by the elements within it. Each element has a different amount of neutron attenuation and accounting for the density of these elements results in a total attenuation for the material. The thickness of material necessary for a 1/e drop in intensity is,

$$d_{I=\frac{1}{e}I_0} = \frac{1}{\sum_i N_A \rho \frac{\sigma_i}{A_i} w_i} \tag{3.1}$$

where i is the ith element of the molecule, N_A is Avogadro's number, ρ is the density of the material, σ_i is the cross-section for the element, A_i is the atomic weight, and w_i is the weight fraction. The thickness for a 1/e drop in intensity of the important materials on the OHPs is shown in Table 3.1. Neutron radiography allows visual observation of the

fluid motion within the OHP because the neutron attenuation of the hydrogen component of water is much higher than that of the metals and nanoparticles used in the OHP. In addition, the density difference between the liquid and vapor phases is easily detectible in the resulting images because only 0.11 cm of liquid water results in the same neutron intensity loss as 4.19 m of water vapor. Therefore, in the images, liquid water blocks most neutrons from reaching the detector, while water vapor, diamond nanoparticles, copper, and aluminum allow many more to pass through and reach the detector.

Table 3.1. Thickness of material necessary for a 1/e loss in neutron beam intensity [26,27]

Material	**Location in OHP**	$d_{I=\frac{1}{e}I_0}$ **(cm)**
Water – Liquid	OHP working fluid	0.11
Water – Vapor	OHP working fluid	4190.64
Carbon – Diamond	Nanoparticles in fluid	0.62
Copper	Tubing and heat spreading plates	0.60
Aluminum	Water cooled blocks and insulation covering	5.76
Silica (approximate fiberglass density)	Fiberglass insulation	277.8

The previous experimental setup for temperature measurements was used with the neutron radiography experiment. Neutron radiography however introduced additional equipment to obtain the video data. Figure 3.4 shows the experimental setup. The OHP was placed between the camera and the beam port on an adjustable test stand. Neutron

masks were positioned in front of the OHP to prevent unnecessary irradiation and the remainder of the equipment was placed outside the neutron shield. Power was supplied to the OHP heater via a Staco 3PN1010B power supply and the OHP was cooled via a Julabo F34/MD circulator. The temperature and video data was acquired by Computer 1 and Computer 2, respectively. Computer 2 acquired the 16 bit images at 30 fps and Computer 1 recorded the temperature data via the National Instruments SCXI 1600 DAQ. The temperature sample rate varied from 50-250 Hz depending on the length of the test. At the beginning of each test the image acquisition software in Computer 2 triggered the temperature DAQ so that the temperature data and images would be synchronized.

Due to the water cooled design of the OHPs, the cooling water blocked visual observation of the OHP in the condenser region. To reduce irradiation of the cooling water and unnecessary irradiation of the OHP, the mask was adjusted to block this region from the neutrons.

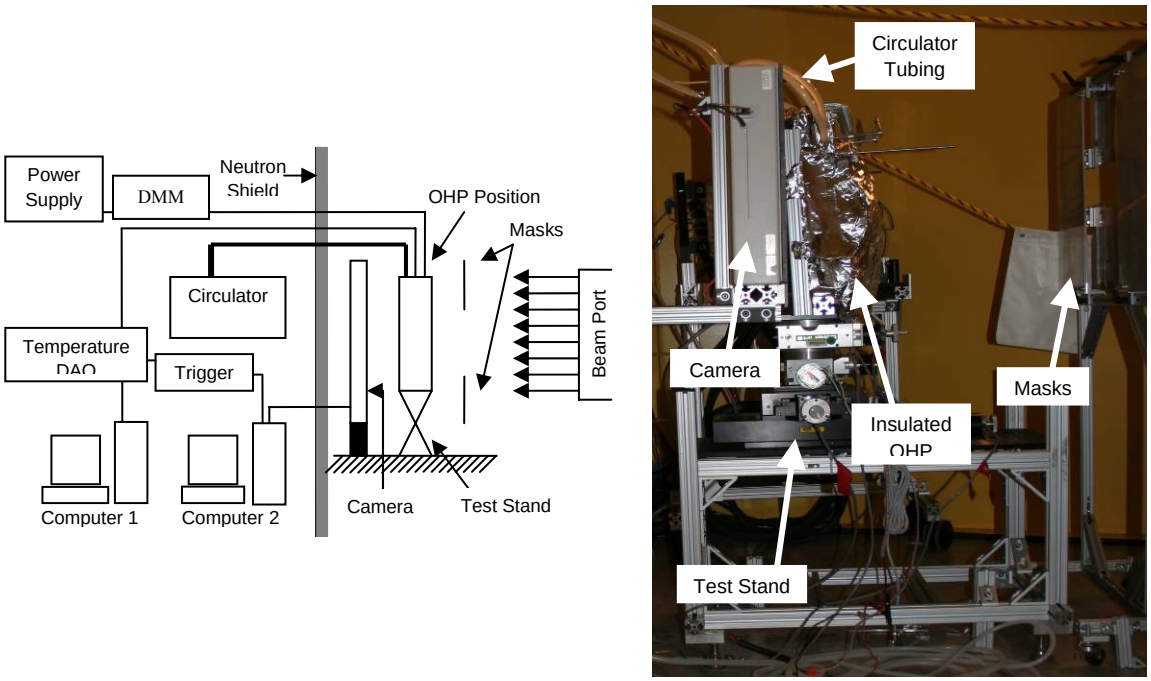

(a) (b)

Fig. 3.4. Neutron radiography (a) schematic of experimental setup and (b) photo of experimental setup

The three OHPs were tested with this setup. They were positioned vertically with the evaporator below the condenser. The OHPs were insulated with aluminum foil encased fiberglass insulation. The aluminum foil prevented the irradiated fiberglass from becoming airborne.

After the video data was acquired, several adjustments were made to the video images. The images were darkfield and brightfield corrected and they were contrast adjusted to increase definition between the fluid and vapor regions. Figure 3.5 illustrates the resulting neutron radiography images. The resulting images had a major limitation, the liquid-vapor interface blurred in the OHPs if it was moving faster than 1 pixel/0.033 seconds. This created problems accurately calculating the fluid velocity.

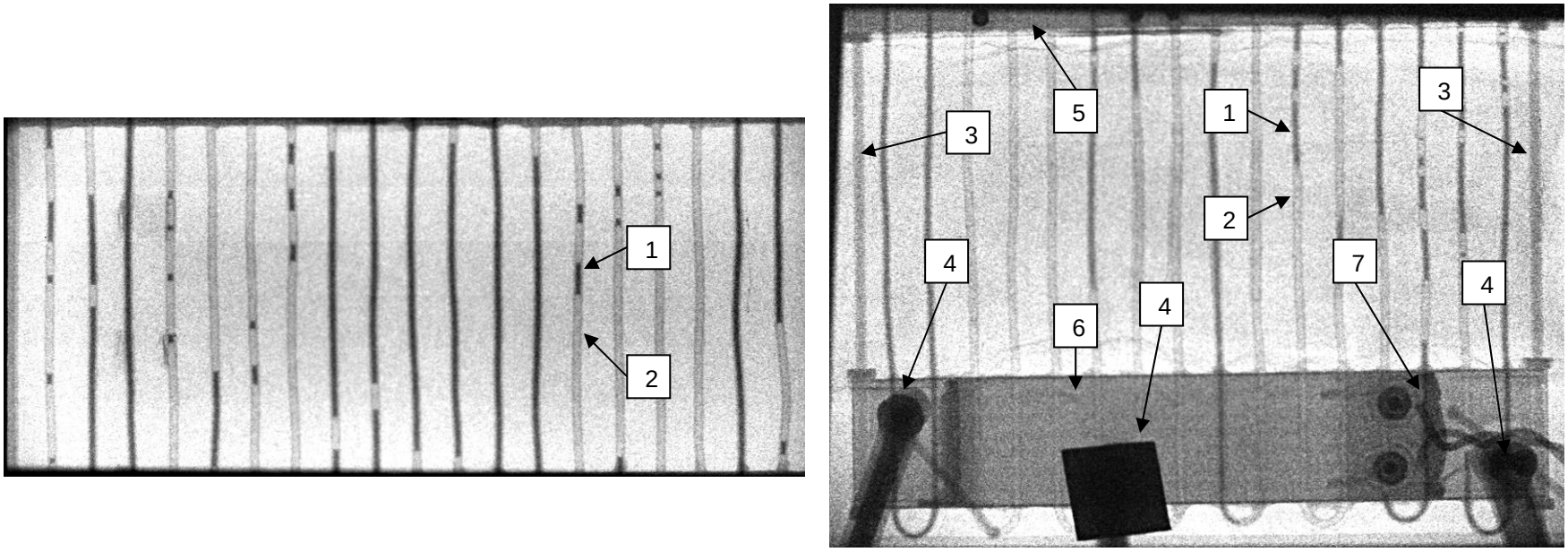

(a) (b)

Fig. 3.5. Neutron radiographic images of (a) 12 turn OHP and (b) 8 turn OHPs (1 is liquid water, 2 is water vapor, 3 is a threaded steel rod used for structural support, 4 is an aluminum clamp used to attach the strip heater to the evaporator, 5 is the condenser, 6 is the strip heater and the evaporator copper plate, and 7 is the strip heater wiring)

Results and Discussion

Using the experimental setup and procedures described above, the heat transport capability in the OHPs were investigated including the effects of nanofluid, operating temperature, gravitational orientation, and transient responses of the OHP.

Figure 3.6 shows the nanofluid effect on the thermal resistance in the 12-turn OHP. The thermal resistance is defined as,

$$R = \frac{T_e - T_c}{Q} \tag{3.2}$$

where T_e is the average evaporator temperature, T_c is the average condenser temperature, and Q is the heat input. As shown, when the OHP was charged with nanofluids, the thermal resistance significantly declined. No other aspect of the OHP was changed therefore this large reduction in thermal resistance was due to the nanoparticles added to the base fluid. However, the thermal conductivity and/or convection coefficient of nanofluid are not known because the oscillating motion actively suspends the nanoparticles and as was shown in Chapter 2 the thermal conductivity of actively suspended nanoparticles can not be measured with typical methods. It can be inferred that the increased thermal conductivity of the settled nanofluid, found with the transient hot-wire method, would result in a similarly increased thermal conductivity of an actively suspended nanofluid.

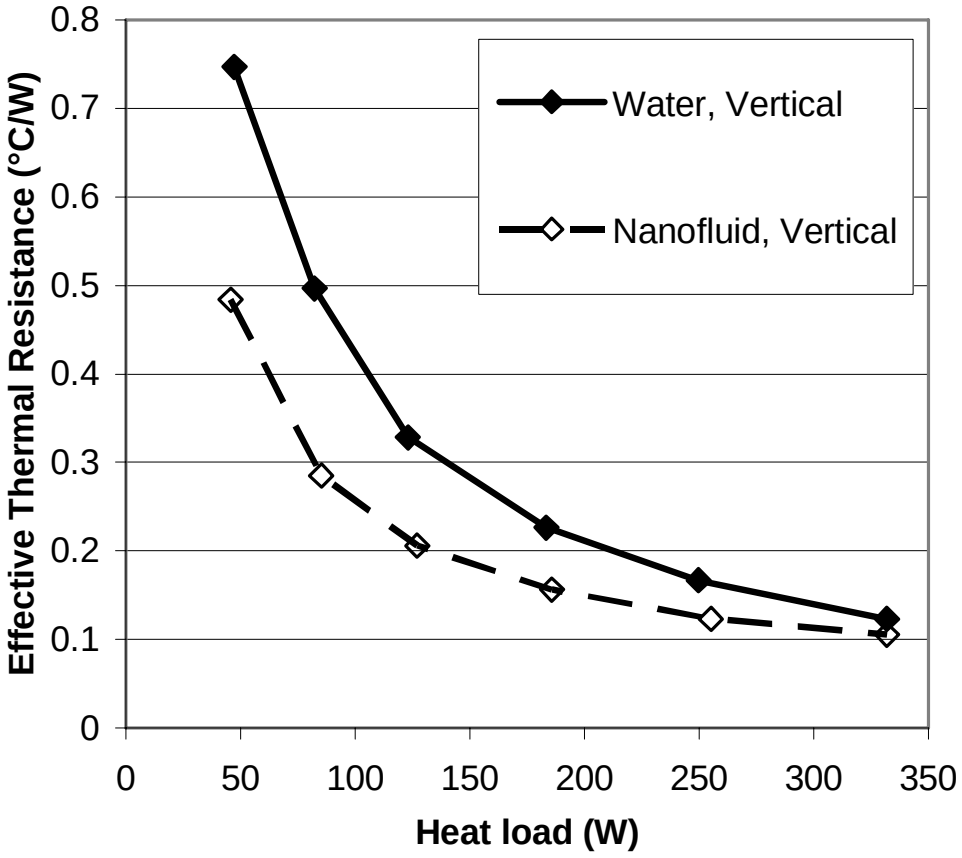

Fig. 3.6. Nanofluid effect on the heat transport capability in a 12-turn OHP (The OHP was vertically oriented with bottom heating and circulator temperature of 20°C)

For both OHPs either charged with pure water or nanofluid, there existed a startup heat input. When the heat input was less than this required startup amount, no oscillating motions were observed and the temperature difference between the evaporator and condenser increased linearly as the power input increased. Once the oscillating motion began in the OHP, the further increase of power input did not significantly increase the temperature difference as shown in Fig. 3.7. When the heat input was too low to create oscillating motion, most nanoparticles would settle down and stay in the evaporating

section. This might partially cause the higher heat resistance at low heat loads (Fig. 3.7). At high heat loads, oscillating motion occurs, suspending the nanoparticles in the fluid and resulting in a significantly reduced thermal resistance. The suspension of the nanoparticles by the oscillation motion of vapor bubbles and liquid plugs is the primary reason for the enhanced heat transport capability in nanofluid OHPs.

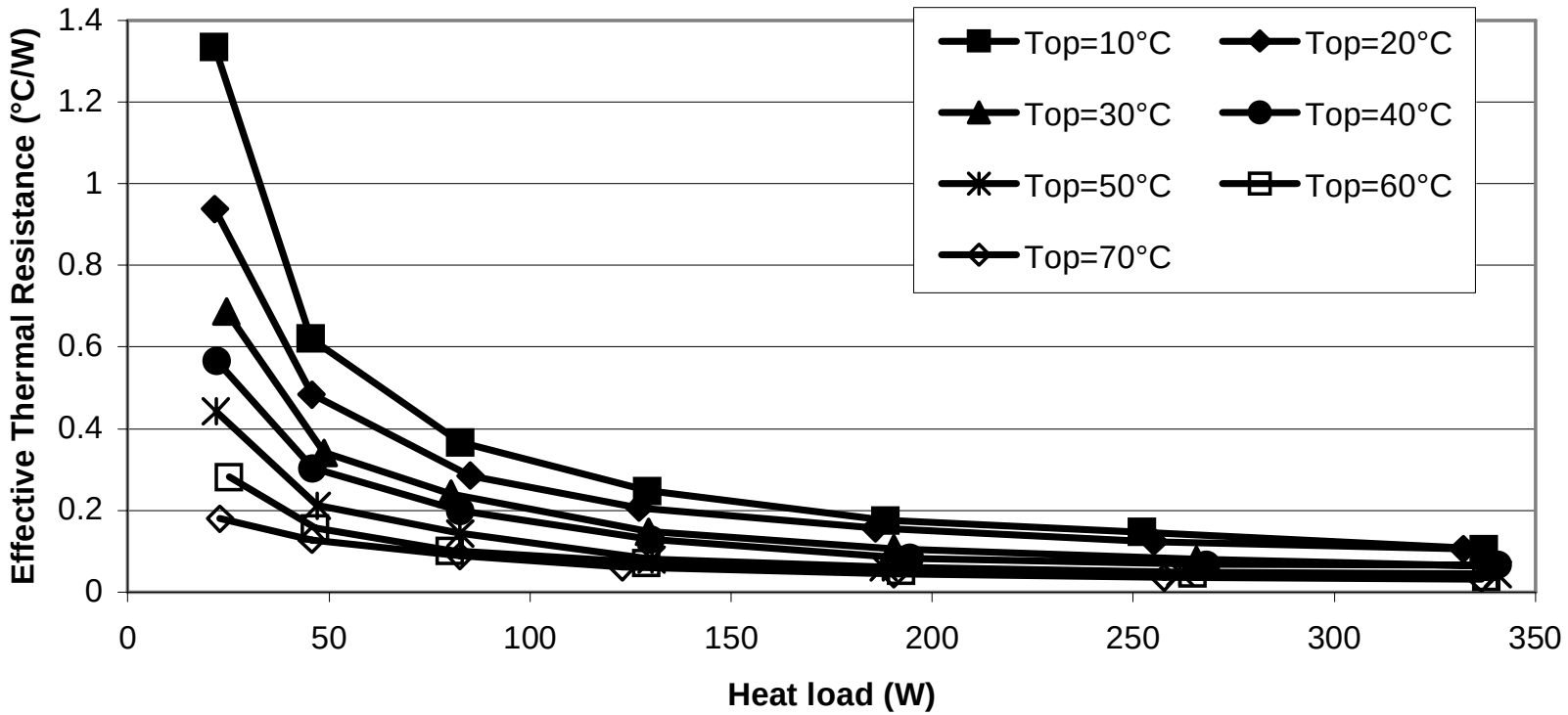

Fig. 3.7. Thermal resistance at various heat loads and operating temperatures of the 12-turn nanofluid OHP oriented vertically with bottom heating

Figures 3.7 and 3.8 show the operating temperature effect on the 12-turn nanofluid OHP. Figure 3.7 shows when the operating temperature increases, the thermal resistance significantly decreased. When the operating temperature was at 70 °C, the thermal resistance occurring in this OHP reached 0.03 °C/W at a total heat input of 336 W. Figure 3.8 shows the operating temperature effect on the temperature difference between the evaporator and condenser. As shown, when the operating temperature increased, the temperature difference between the evaporator and condenser significantly decreased. For example, when 255 W was added to the evaporator, the temperature difference was 31.4 °C at an operating temperature of 20 °C. When the operating temperature increased to 70 °C, the temperature difference was reduced to 9.2 °C. If the heat transfer rate from the evaporator to the condenser is expressed as $Q = UA(T_e - T_c) = (T_e - T_c)/R$, the overall heat transfer coefficient (UA) increases from 8.13 W/°C at 20 °C to 27.8 W/°C at 70 °C. In other words, the overall heat transfer coefficient increased 3.4 times when the operating temperature increased from 20 °C to 70 °C.

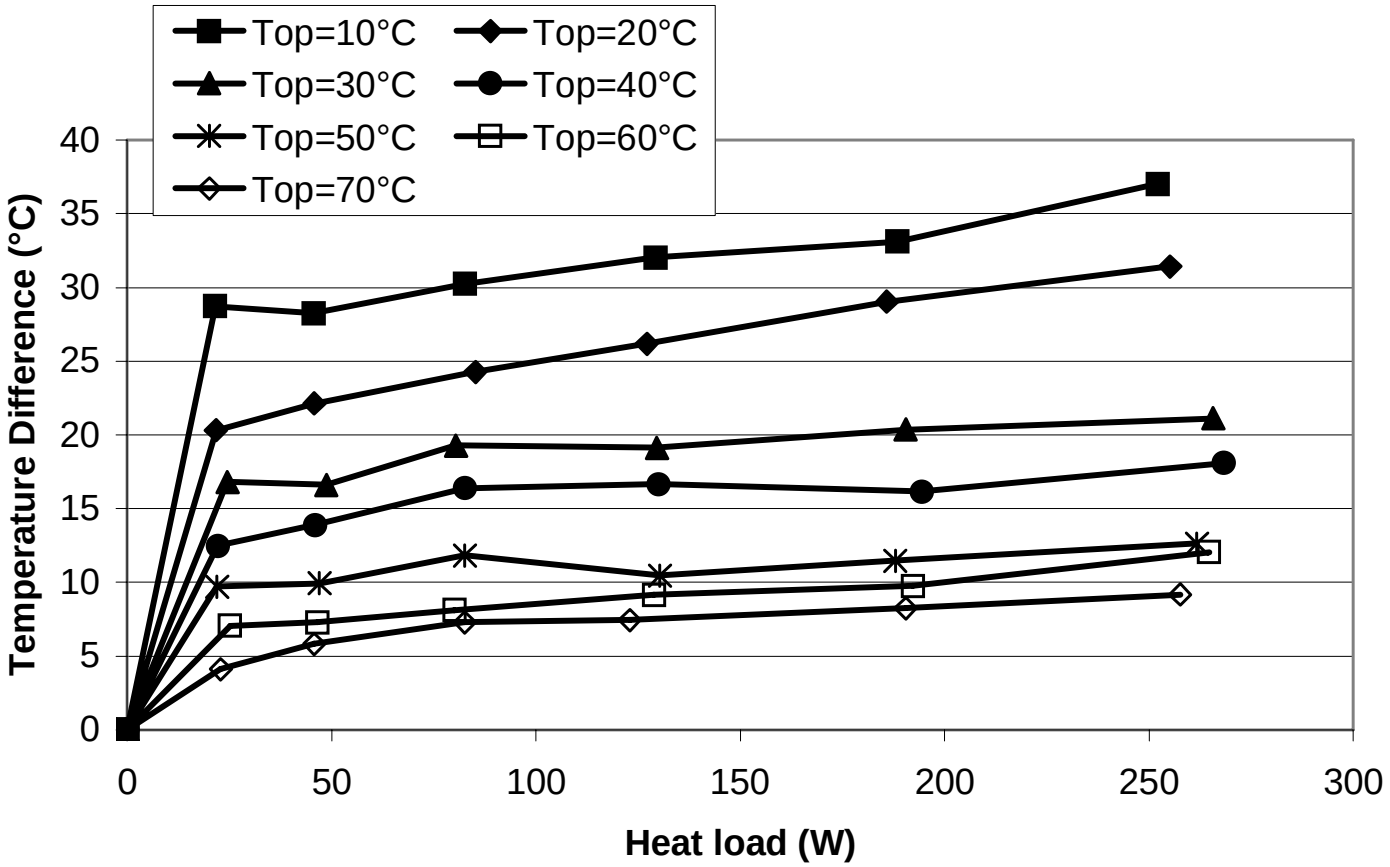

Fig. 3.8. Operating temperature effect on the temperature difference between the evaporator and condenser of the 12-turn nanofluid OHP oriented vertically with bottom heating

The operating temperature also affects the transient response of the OHP as shown in Figs. 3.9 and 3.10. For the same heat load, the 10 °C operating temperature has a much sharper transition from start-up to oscillating motion. At 66.7 °C, there is a very smooth transition however steady-state is reached later than at 10 °C.

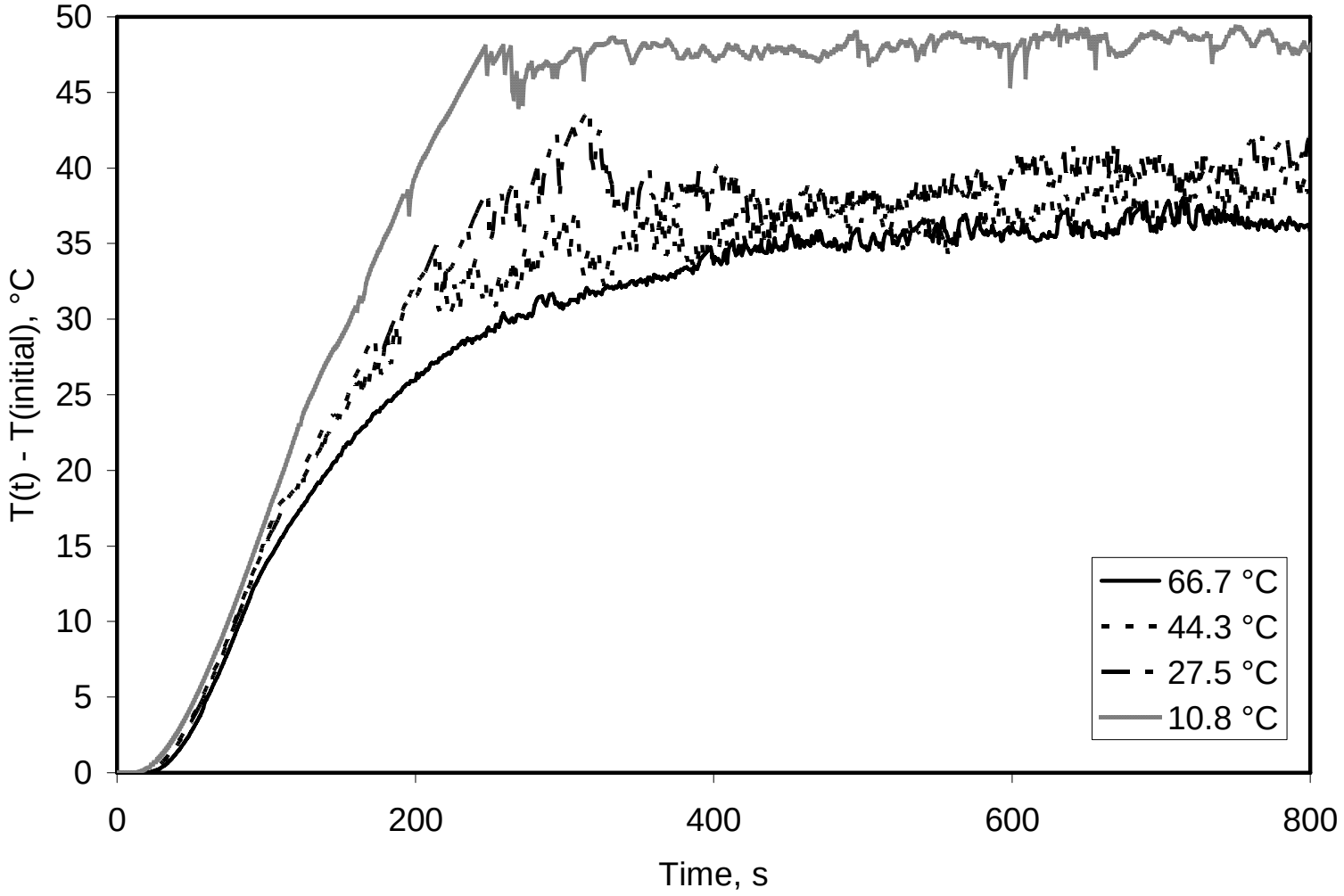

Fig. 3.9. Evaporator transient temperature response of the 12-turn nanofluid OHP with a 336 W step heat input at t = 0

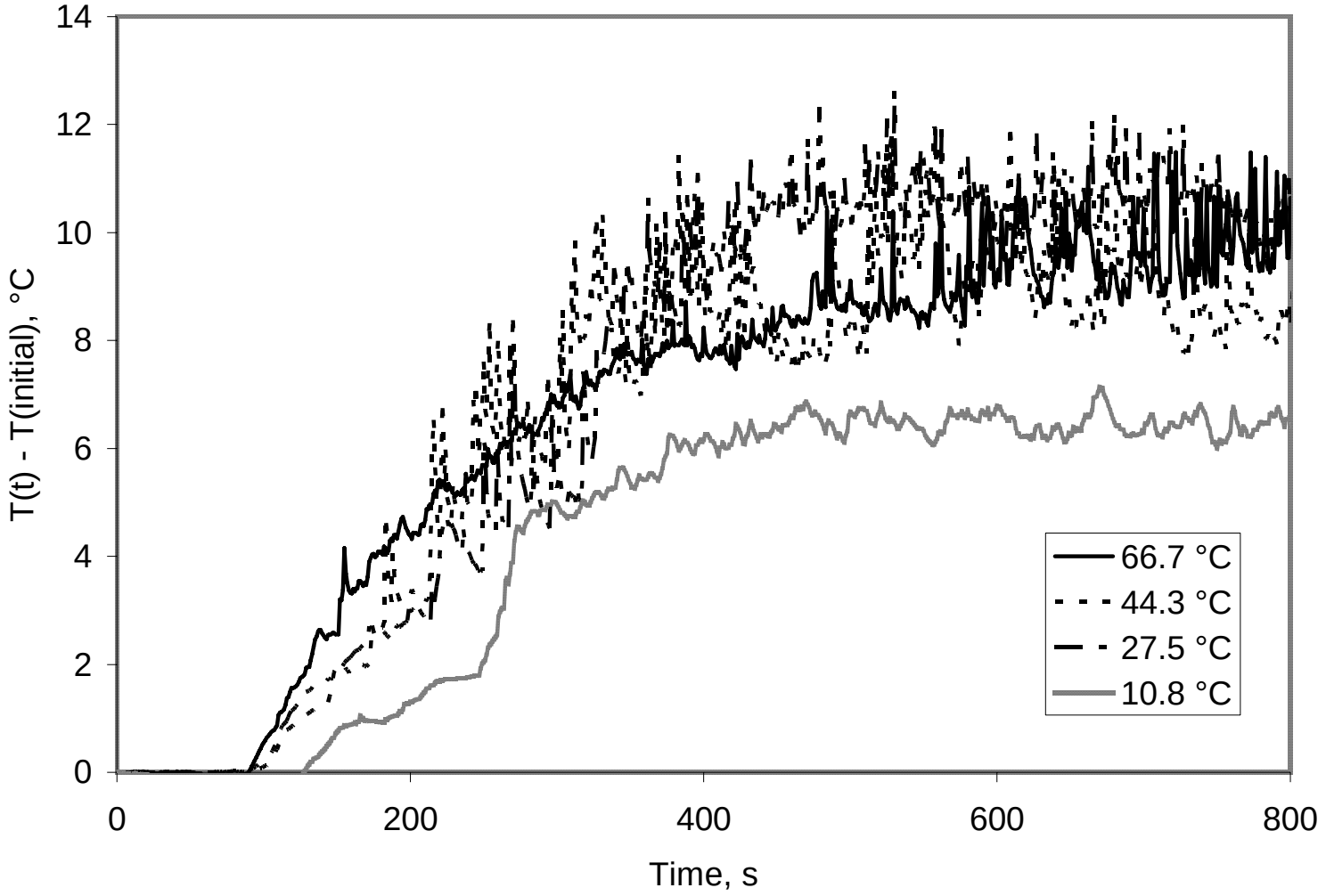

Fig. 3.10. Condenser transient temperature response of the 12-turn nanofluid OHP with a 336 W step heat input at t = 0

The effect of gravitational orientation on the 12 turn nanofluid and water OHP is shown in Fig. 3.11. The vertical orientation resulted in the lowest temperature difference with the 45° orientation only slightly worse. The horizontal orientation had by far the highest temperature difference. The effect of gravity on the OHP temperature difference is essentially the same for the water and nanofluid OHP, in the horizontal, vertical and 45° orientations. The temperature difference between the water and nanofluid OHP at these orientations is approximately 9 °C at 255 W. At low heat loads before oscillations begin, the nanofluid and water OHP exhibit essentially the same temperature differences.

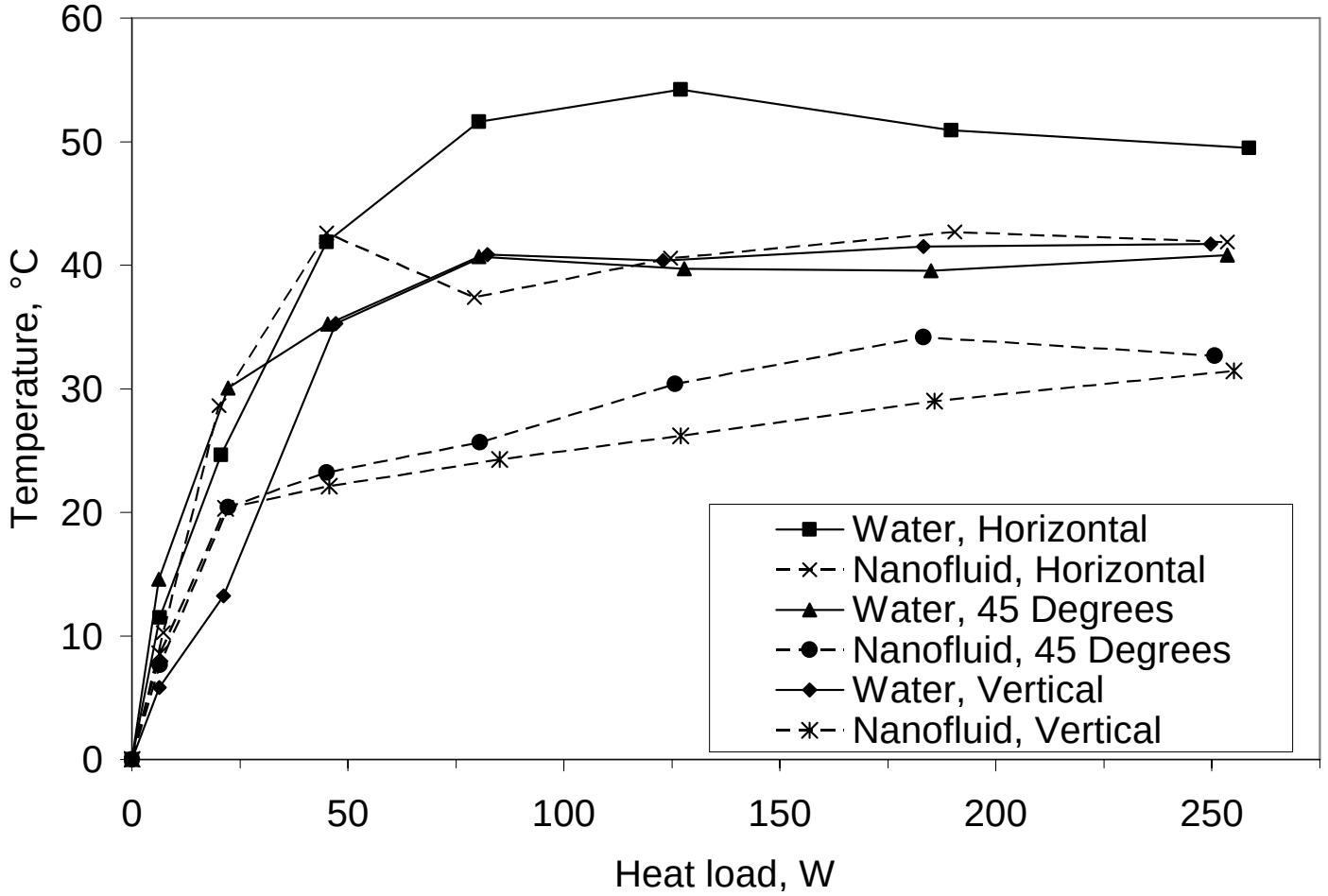

Fig. 3.11. Average temperature difference at different angles for the 12-turn water and nanofluid OHP (for the 45° and vertical orientations, the evaporator is gravitationally below the condenser)

Figure 3.12 shows the effect of operating temperature on the water and nanofluid 8-turn OHP. The temperature difference between the 8-turn water and nanofluid OHP are less than the 12 turn water and nanofluid OHP, however this is likely due to 8 turn OHP having a much lower nanofluid vol% than the 12 turn OHP. At lower operating temperatures, the nanofluid has a significant effect on the OHP, however above 60 °C the nanofluid and water 8 turn OHPs perform similarly.

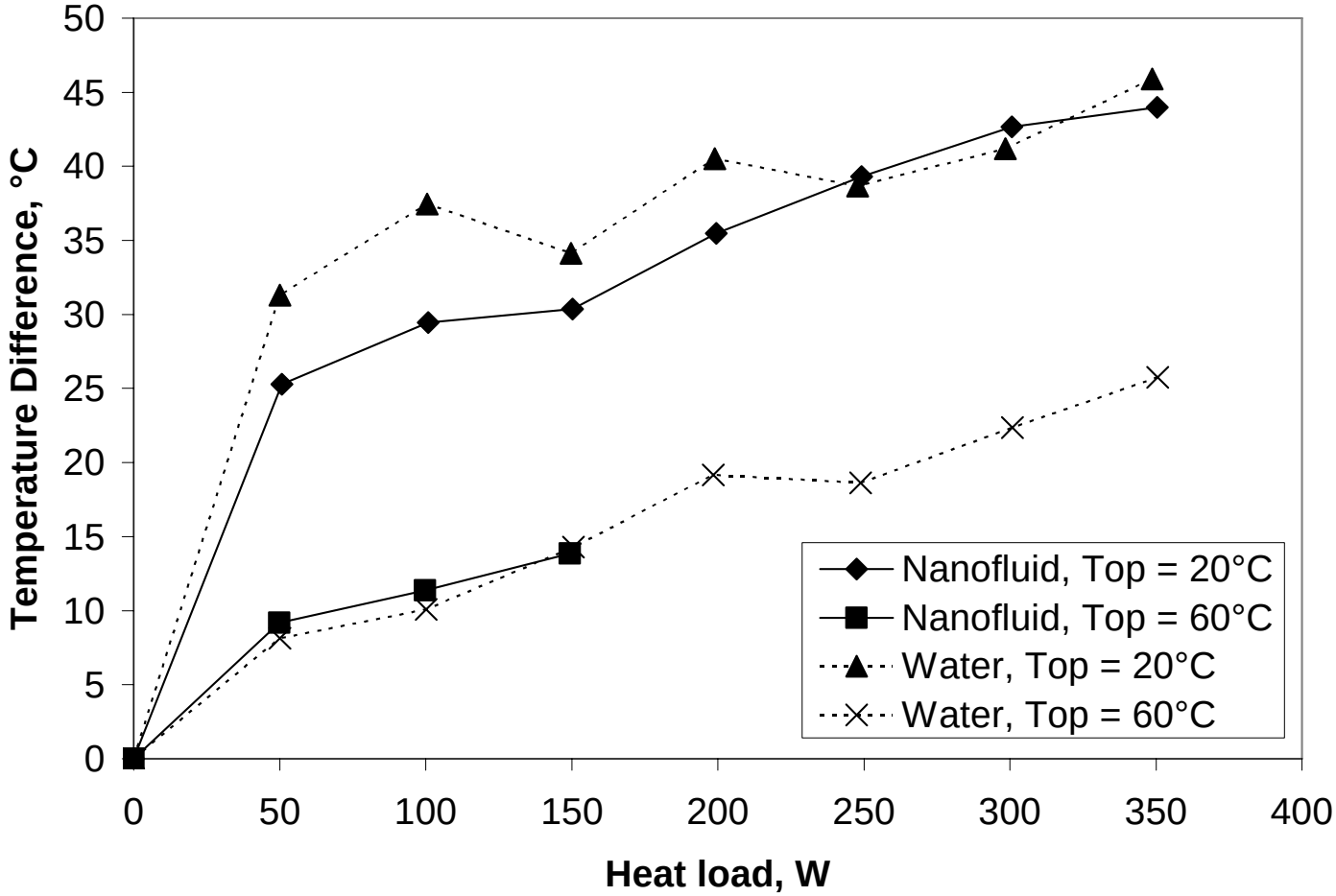

Fig. 3.12. Operating temperature effect on the temperature difference of the 8-turn water and nanofluid OHP

Figures 3.13 and 3.14 shows the transient temperature responses in the evaporator and condenser at heat inputs of 123 W and 336 W. When the operating temperature increased, the transient temperatures on the evaporator and condenser were smoother. This indirectly shows that when the operating temperature increased, the oscillating amplitudes were larger and/or the oscillating frequencies were higher. This is because at high frequencies and larger amplitudes, the thermal diffusivity of the copper tubing results in the thermocouples measuring a dampened temperature oscillation compared to the actual temperature oscillations of the fluid. When the operating temperature increases, higher thermal conductivity, lower viscosity of nanofluid, and larger oscillating amplitude might be the primary factors enhancing the heat transport capability in a nanofluid oscillating heat pipe.

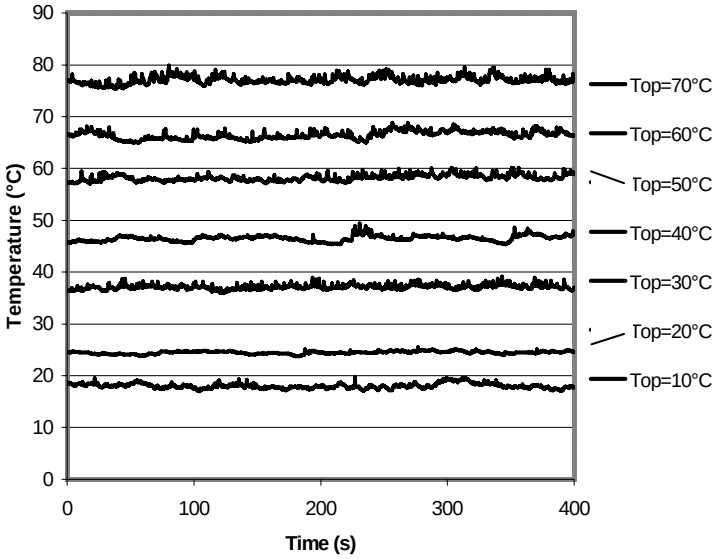

(A)

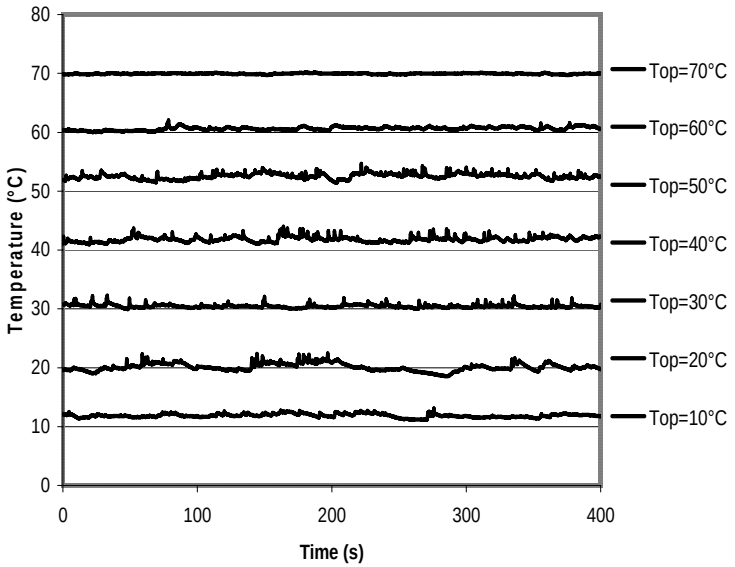

(B)

Fig. 3.13. Operating temperature effect on the temperature fluctuations in the evaporator at a heat input of 123 w (a) evaporator and (b) condenser of the 12-turn nanofluid OHP with bottom heating

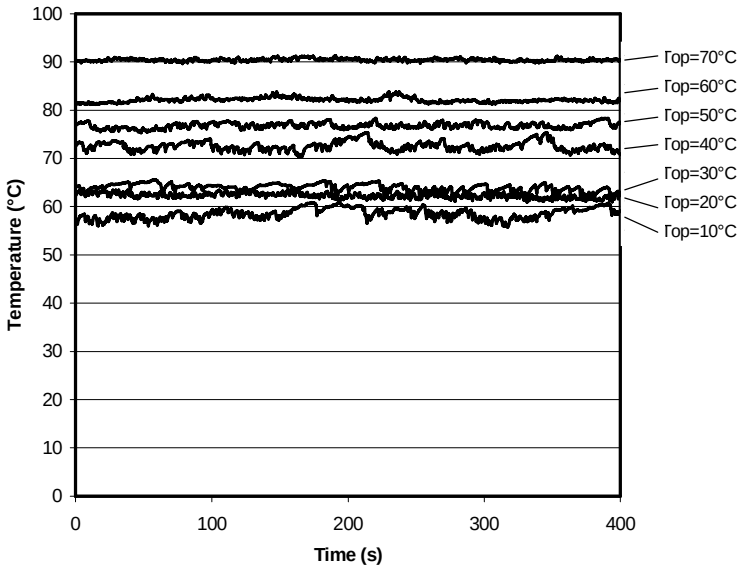

(A)

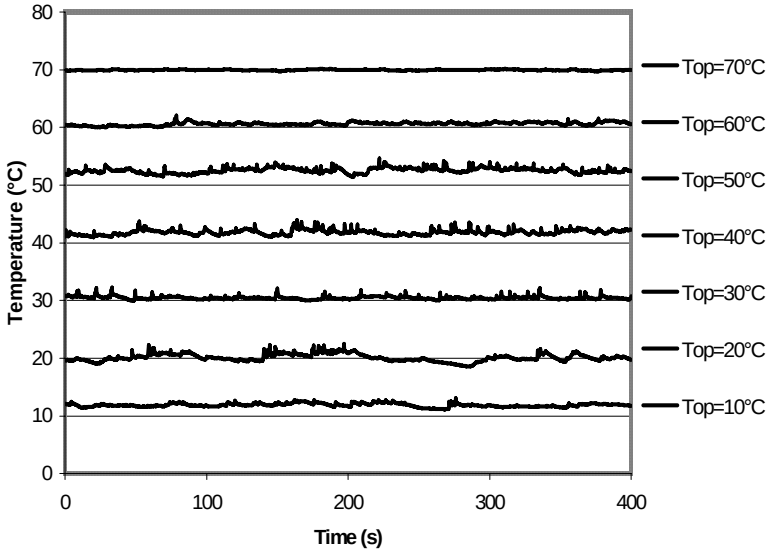

(B)

Fig. 3.14. Operating temperature effect on the temperature fluctuations at a heat input of 336 w (a) evaporator and (b) condenser of the 12-turn nanofluid OHP oriented vertically with bottom heating

Neutron Radiography Results and Discussion

Neutron radiography allowed the fluid motion patterns and trends to be observed in the OHPs. Several of these will be discussed in detail: the transient startup process, fluid motion at varying heat loads, and oscillating motion comparisons for the 8-turn water and nanofluid OHP and the 12-turn nanofluid OHP.

The transient startup stages of the OHPs are illustrated by a test on the 12-turn OHP with a step heat input of 300 W. Four different stages of fluid motion were observed during the transient startup period of the OHP. In stage 1 heat was added to the evaporator at 0 seconds. The vapor plugs expanded within the evaporator slowly pushing the liquid toward the condenser (Fig. 3.15: t = 0, 5, 10 s). During stage 2, occurring at about 15 seconds, the evaporator pressure was high enough in some turns to slowly push liquid and vapor in other turns from the condenser toward the evaporator region (Fig. 3.15: t = 15, 25, 35, 45 s). Stage 3 began around 50 seconds and was characterized by some very slow flow reversals (Fig. 3.15: t = 50, 55, 60 s). At 1 minute, stage 4, there was a sudden transition to oscillating behavior (Fig. 3.15: t = 60, 65, 70, 75 s). This oscillation motion occurred very quickly and occurred throughout the heat pipe. During all of these stages, the temperature response was very smooth and the fluid oscillations were barely noticeable in the temperature measurements (Fig. 3.16). Beyond stage 4, oscillating motion in the OHP steadily increased in velocity and amplitude until the temperature reached steady state. At about 2 minutes, temperature oscillations were observed on the surface of the OHP, however there is no discernable change in the flow pattern. This does not necessarily imply the flow pattern remained the same, only that

flow pattern changes might not be visible for the OHPs because of the limitations of the neutron radiography images.

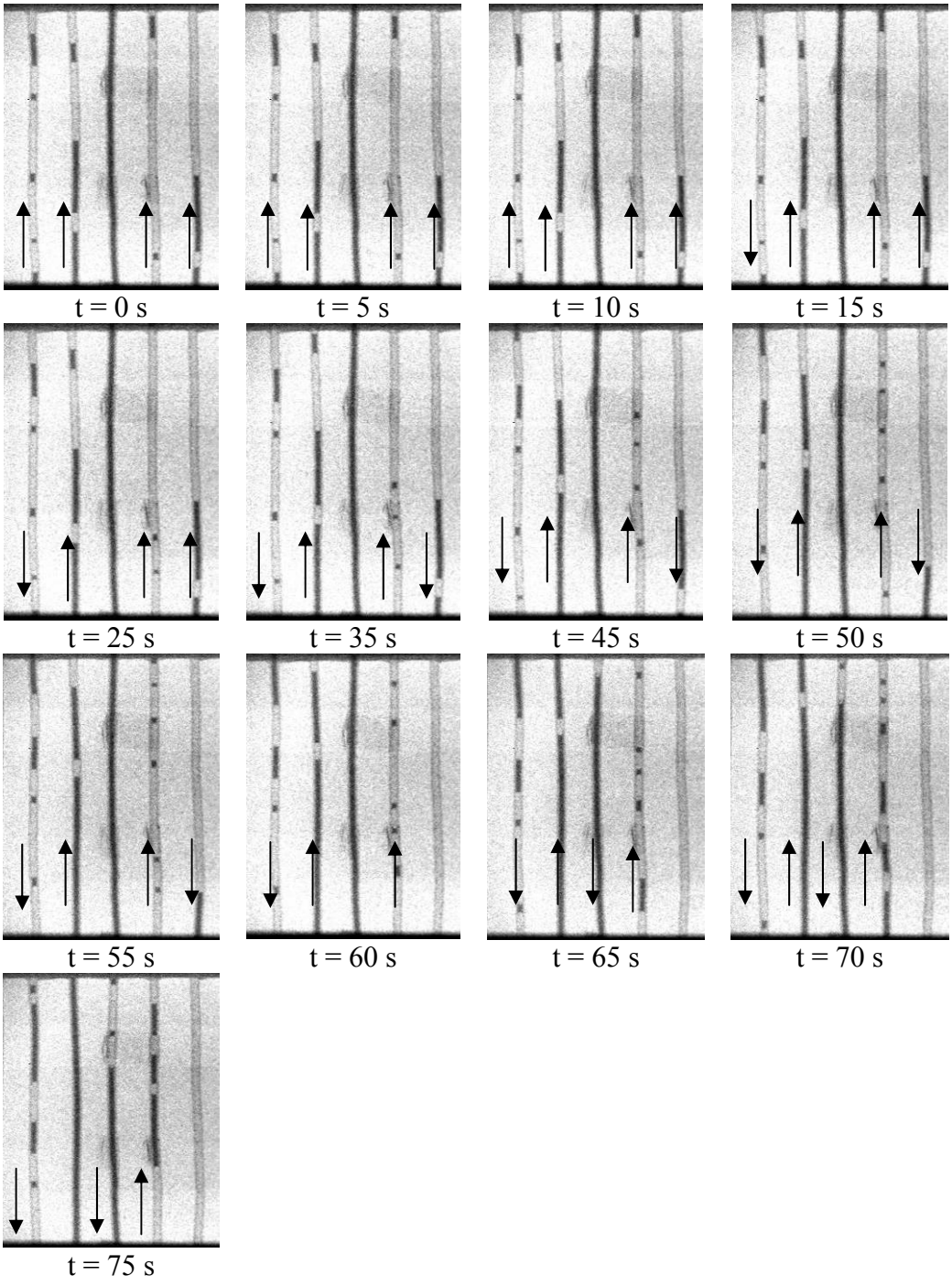

Fig. 3.15. Flow direction with time of the 12-turn nanofluid OHP with a 300 W step input at t = 0 s (Flow direction for each tube is noted with an arrow)

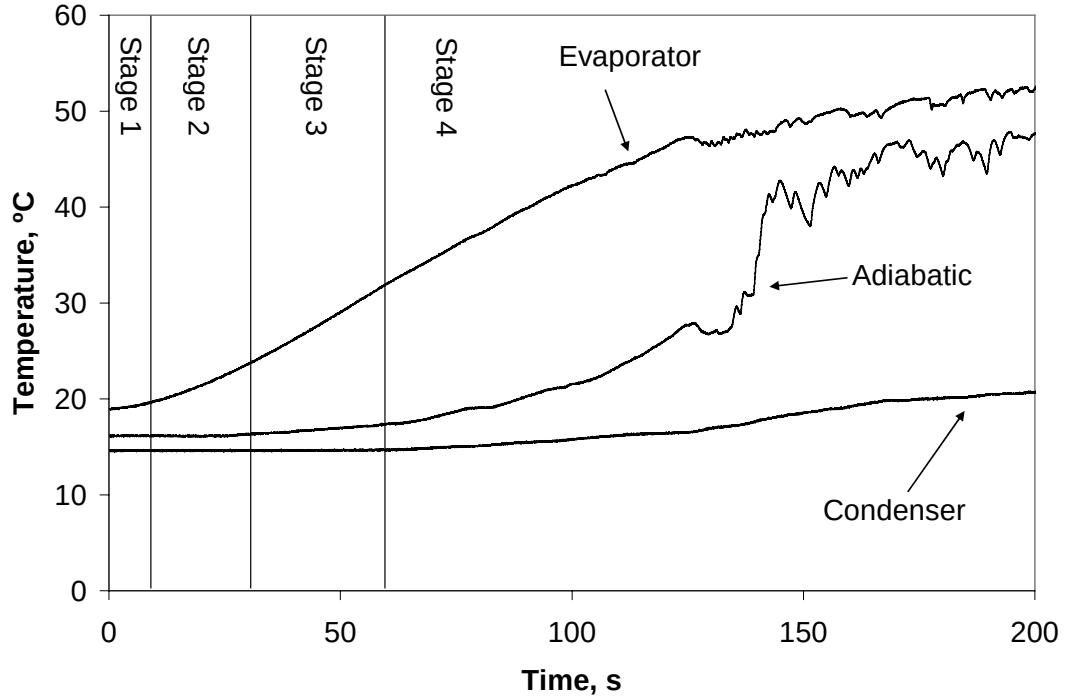

Fig. 3.16. Temperature response of the 12-turn nanofluid OHP subjected to a step heat input of 300 W

The flow characteristics of the different OHPs were very similar. They were characterized by fast fluid movement at the center turns of the OHP, very little movement in the outer turns, and almost no bulk flow. This is illustrated in Fig. 3.17 with the 8-turn nanofluid OHP at 199.5 W. This flow distribution in the 8 and 12-turn OHPs was likely due to a non-uniform heat flux provided by the strip heater. The outer turns of the OHP received a lower heat flux while the inner turns received a higher heat flux. Besides to the non-uniform movement of the OHPs, each OHP exhibited slightly different flow patterns. At the same heat load and operating temperature, each heat pipe behaved slightly differently. The 12-turn nanofluid OHP had the lowest frequency and amplitude. The heat flux per tube of the 12-turn OHP was lower than the 8-turn OHPs, therefore should result in a lower frequency and amplitude. Also, the 8-turn nanofluid OHP had a

lower frequency and amplitude than the 8-turn water OHP. The high thermal conductivity of the nanofluid OHP transferred more heat per slug of liquid and therefore allowed the OHP to transfer the same amount of heat with less movement.

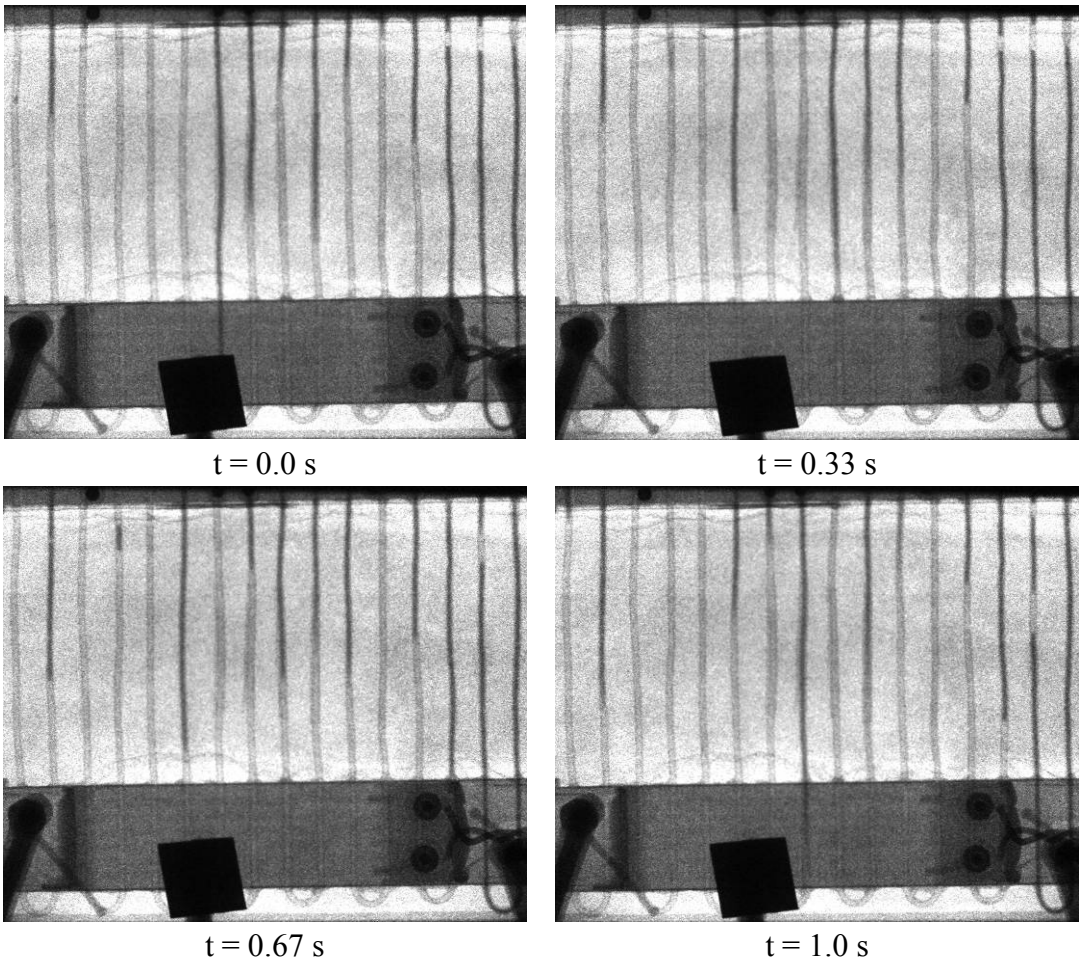

Fig. 3.17. Non-uniform flow in the 8-turn nanofluid OHP at 199.5 W

Increasing the heat load of the OHPs caused a noticeable increase in fluid velocity and oscillating amplitude. This is illustrated with the 12-turn nanofluid OHP at 50.5 W (Fig. 3.18) and 199.4 W (Fig. 3.19). For the 12-turn nanofluid OHP at 50.5 W, the fluid moved very slowly with only minor movements. At 199.4 W, the fluid movement was

much faster. This is observable in Fig. 3.19 by the blurring occurring in these images. Because each image capture lasted 1/30th of a second, this blurring is the result of the fluid moving a substantial distance during that time interval.

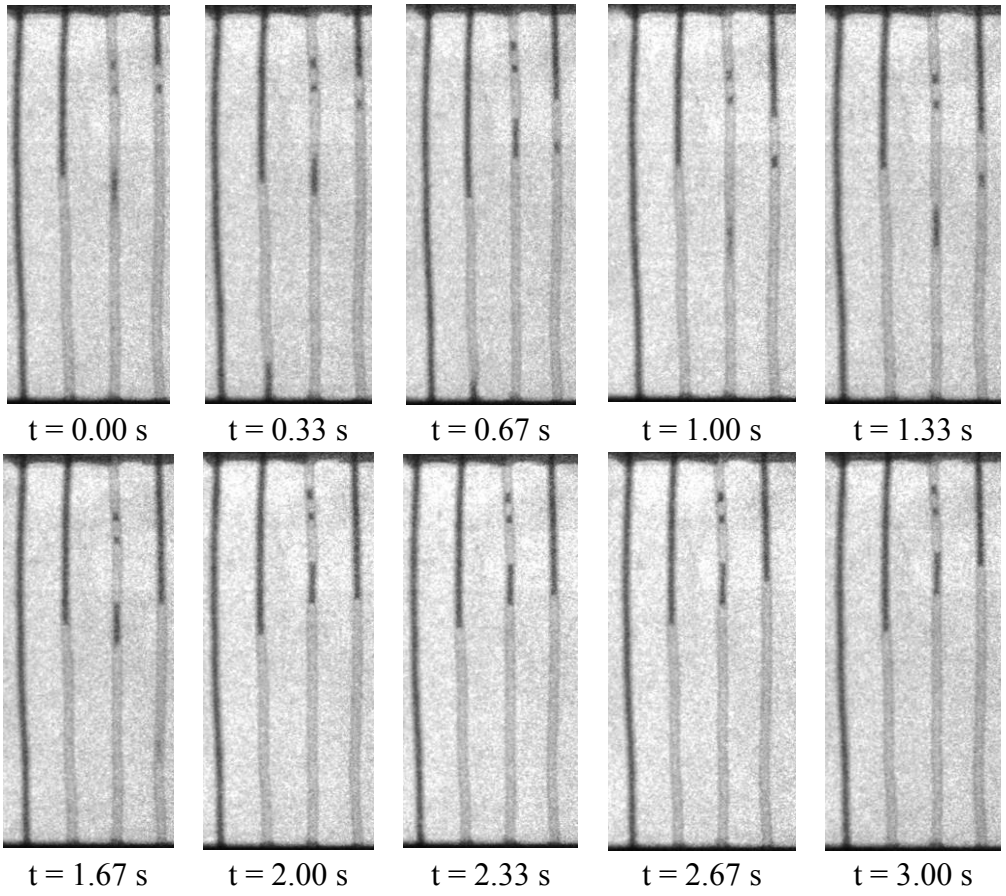

Fig. 3.18. Fluid movement in the center turns of the 12-turn nanofluid OHP at 50.5 W and an operating temperature of 20 °C

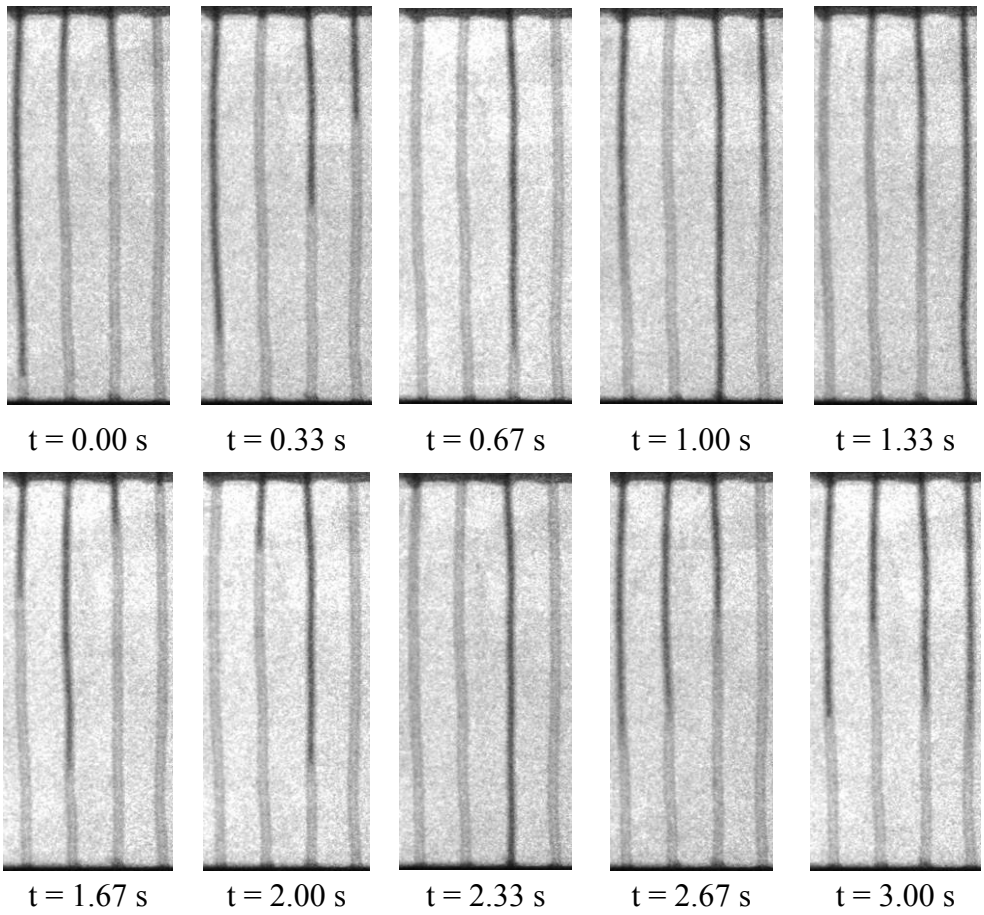

Fig. 3.19. Fluid movement in the center turns of the 12-turn nanofluid OHP at 199.4 W and an operating temperature of 20 °C

From a thermal perspective, increasing the operating temperature significantly reduced the temperature difference between the evaporator and condenser. Visually, the fluid motion for an operating temperature of 60 °C had a higher frequency and amplitude than the fluid motion at 20 °C. This is shown with the 12-turn OHP at an operating temperature of 20 °C and 60 °C in Fig. 3.18 and Fig. 3.20 respectively. Because the fluid velocity change was not as substantial as with increased heat flux, this trend is hard to observe in these figures.

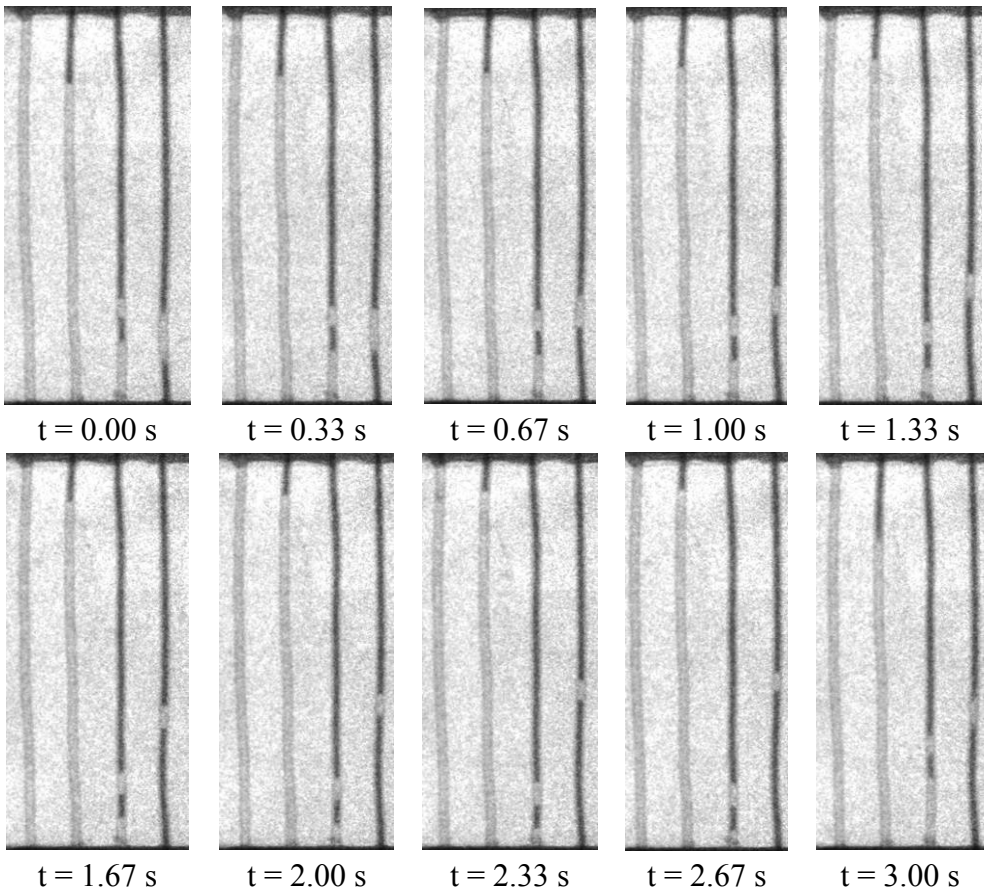

Fig. 3.20. Fluid movement in the center turns of the 12-turn nanofluid OHP at 50.1 W and an operating temperature of 60 °C

Nucleation was never observed in the middle of a liquid slug and only occasionally was a bubble observed to completely condense or a liquid slug to completely evaporate. The lack of nucleation observation is likely due to motion blur of the liquid-vapor interface and the low resolution of the video obscuring these occurrences from being observed. In addition, the condenser region was not visible; therefore it was impossible to determine if vapor bubbles were completely condensing in this region. However, occasionally in the adiabatic region near the condenser, vapor was observed to condense.

CHAPTER 4

CONCLUSIONS

An experimental investigation of OHPs was conducted to determine the nanofluid effect on the heat transport capability in an OHP. Three OHPs were constructed, one 12-turn OHP and two 8-turn OHPs. They were tested with both HPLC grade water and diamond nanofluid. It was found that nanofluid significantly increase the heat transport capability in an OHP. In order to determine the primary factors affecting the heat transfer enhancement of the OHP, the thermal conductivity of the motionless nanofluid was measured. These experimental results show that the diamond nanoparticles can enhance the thermal conductivity of nanofluid. At an ambient temperature of 21 °C, the thermal conductivity for nanofluid was determined to be 1.0 W/m-K comparing with the thermal conductivity of 0.6 W/m-K for HPLC grade water. Therefore, the nanofluid provided a significant increase in thermal conductivity, which is a primary reason for the significantly increased the heat transport capability in the OHP. Another factor investigated was the operating temperature affect on the OHP. It was shown that increased operating temperatures significantly increase the heat transport capability of the investigated OHPs. However when the water and nanofluid OHPs were compared, the nanofluid OHP primarily had an advantage at low heat loads and lower operating temperatures. In these situations, the fluid amplitude and frequency, observed with neutron radiography, was lower than those at higher operating temperatures and heat loads. Neutron radiography also showed that the fluid amplitude and frequency was higher with water OHPs compared to nanofluid OHPs at similar settings. This is likely due to the nanofluid OHPs transferring more heat per unit volume than the water OHPs

and therefore keeping the pressure difference across the OHP lower. In all situations the nanofluid OHPs performed better than the water OHPs. The 12-turn OHP charged with nanofluids achieved the lowest thermal resistance of 0.03 °C/W. The nanofluid OHP investigated here provides a new approach in designing a highly efficient heat pipe cooling device.

REFERENCES

1. Akachi, H., 1990, "Structure of a Heat Pipe," U.S. Patent #4,921,041.

2. Choi S. U. S, 1995, "Enhancing thermal conductivity of fluids with nanoparticles," *Proceedings of the 1995 ASME International Mechanical Engineering Congress and Exposition*, San Francisco, CA, USA.

3. Eastman, J. A. et al., 2001, "Anomalously increased effective thermal conductivities of ethylene glycol-based nanofluids containing copper nanoparticles," *Applied Physics Letters*, Vol. 78, **6**, 718-720.

4. Das, S. K., Putra, N., Thiesen, P., Roetzel, W., 2003, "Temperature dependence of thermal conductivity enhancement for nanofluids," *ASME Journal of Heat Transfer*, Vol. 125, 567-574.

5. Wen D S, Ding Y L, Mar 2005, "Experimental investigation into the pool boiling heat transfer of aqueous based gamma-alumina nanofluids," *Journal Of Nanoparticle Research*, **7**, 265-274

6. Putra N, Roetzel W, Das SK, Sep 2003, "Natural convection of nano-fluids," *Heat and Mass Transfer*, **39**, 775-784

7. Wen D S, Ding Y L, Dec 2005, "Formulation of nanofluids for natural convective heat transfer applications," *International Journal Of Heat And Fluid Flow*, **26**, 855-864

8. Eastman, J. A., Choi, S. U. S., Li, S., Thompson, L. J., Feb 2001, "Anomalously increased effective thermal conductivities of ethylene glycol-based nanofluids containing copper nanoparticles," *Applied Physics Letters*, Vol. 78, **6**, 718-720.

9. Qu, W., Fu, Z., Ma, T., 2004, "Thermal analysis of a micro or mini pulsating heat pipe," *13th International Heat Pipe Conference (13th IHPC), Shanghai, China, September 21-25, 2004*, **2**, 178-186.

10. Xu, J. L., Li, Y. X., and Wong, T. N., 2005, "High speed flow visualization of a closed loop pulsating heat pipe," *Heat and Mass Transfer*, **48**, 3338-3351.

11. Khandekar, S., Schneider, M., Schafer, P. Kulenovic, R., and Groll, M., 2002, "Thermofluid dynamic study of flat-plate closed-loop pulsating heat pipes," *Microscale Thermophysical Engineering*, **6**, 303-317.

12. Cai, Q., Chen, R., and Chen, C., 2002, "An investigation of evaporation, boiling, and heat transport performance in pulsating heat pipe," *Proceedings of IMECE2002 ASME International Mechanical Engineering Congress & Exposition*, 99-104.

13. Khandekar, S., and Groll, M., 2004, "An insight into thermo-hydrodynamic coupling in closed loop pulsating heat pipes," *International Journal of Thermal Sciences*, **43**, 13-20.

14. Cao, X., Cheng, P., 2004, "A novel design of pulsating heat pipes with improved performance," *13th International Heat Pipe Conference (13th IHPC), Shanghai, China, September 21-25, 2004*, **1**, 302-307.

15. Li, Y., Xu, J., Li, Y., 2004, "Study of pulsating heat pipe in GIEC, CAS," *13th International Heat Pipe Conference (13th IHPC), Shanghai, China, September 21-25, 2004*, **1**, 321-328.

16. Karimi, G., and Culham, J. R., 2004, "Review and assessment of pulsating heat pipe mechanism for high heat flux electronic cooling," *2004 InterSociety Conference on Thermal Phenomena*, 52-59.

17. Shafii, M., Faghri, A., and Zhang, Y., 2001, "Thermal Modeling of Unlooped and Looped Pulsating Heat Pipes," *ASME Journal of Heat Transfer*, Vol. 123, 1159-1172.

18. Khandekar, S., Cui, X., and Groll, M., 2002, "Thermal Performance Modeling of Pulsating Heat Pipes by Artificial Neural Network," *Heat Pipe Science Technology Application, Proceedings of the 12th International Heat Pipe Conference, Moscow, Russia, May 19-24*, 215-219.

19. Zhang, X. M., Xu, J. L., and Zhou, Z. Q., 2004, "Experimental study of a pulsating heat pipe using FC-72, ethanol and water as working fluids," *Experimental Heat Transfer*, **17**, 47-67.

20. Wang, S., and Nishio, S., 2005, "Heat transport characteristics in closed loop oscillating heat pipes," *2005 ASME Summer Heat Transfer Conference July 17-22, 2005, San Francisco, California, USA*.

21. Nikkanen, K., Lu, C. and Kawaji, M., 2005, "Effects of working fluid, fill ratio, and orientation on looped and unlooped pulsating heat pipes," *2005 ASME Summer Heat Transfer Conference July 17-22, 2005, San Francisco, California, USA*.

22. Ha, S., Park, C., Kim, J., 2004, "Heat transfer performance of oscillating capillary tube heat pipe with micro-channel flat tube," *13th International Heat Pipe Conference (13th IHPC), Shanghai, China, September 21-25, 2004*, **2**, 194-199.

23. Tye, R. P., 1969, Thermal Conductivity, Vol. 2, Academic Press Inc., New York, Chap. 1-2.

24. Wakeham, W. A., Nagashima, A., Sengers, J. V., 1991, Measurement of the Transport Properties of Fluids: Experimental Thermodynamics, Vol. 3, Blackwell Scientific Publications, Boston, 113-194.

25. Kang, U. H., Kim, S. H., and Oh, J. M., 2006, "Estimation of thermal conductivity of nanofluid using experimental effective particle volume," *Experimental Heat Transfer*, **19**, 181-191.

26. Wilson, A. J. C., 1992, International Tables for Crystallography, Vol. C, Kluwer Academic Publishers, Boston, 384-385.

27. Incropera, F. P., DeWitt, D. P., 2002, Introduction to Heat Transfer, 4th ed., John Wiley & Sons, New York.